JOURNAL OF GEOPHYSICAL RESEARCH, VOL. 111, A06206, doi:10.1029/2005JA011366, 2006

Substorms during the 10–11 August 2000 sawtooth event

M. G. Henderson,[1] R. Skoug,[1] E. Donovan,[2] M. F. Thomsen,[1] G. D. Reeves,[1]
M. H. Denton,[1,3] H. J. Singer,[4] R. L. McPherron,[5] S. B. Mende,[6] T. J. Immel,[6]
J. B. Sigwarth,[7] and L. A. Frank[8]

Received 16 August 2005; revised 9 February 2006; accepted 16 February 2006; published 14 June 2006.

[1] Sawtooth events have been identified at geosynchronous orbit as large-amplitude quasiperiodic (2–4 hour period) modulations of the energetic electron and ion fluxes. They are called sawtooth events because the shape of the flux versus time profiles are composed of rapid increases followed by gradual decreases that resemble the teeth on a saw blade. Although much of the phenomenology associated with sawtooth events is substorm-like, there is still debate as to whether the individual teeth are substorms or not. Here we examine each of the teeth associated with the 10–11 August 2000 sawtooth event in detail. We find that all but one of the teeth were associated with injections at geosynchronous orbit and that most of the teeth were consistent with the hypothesis that they are predominantly caused by unusually large and longitudinally extended substorms. A few were unclear or complex, and the final flux enhancement at 1845:36 UT was not a substorm but a solar wind shock-associated disturbance. In addition, the presence of numerous dispersionless flux perturbations in the LANL SOPA data provides support for the hypothesis that solar wind pressure variations can modulate the flux profiles to some extent. For the substorm events we find that the geosynchronous particle injections were neither globally simultaneous nor globally dispersionless but were instead consistent with a nightside/duskside source in most cases. Similarly, we show that the field dipolarizations were also not global and simultaneous. Each of the substorms was also associated with high-latitude negative H bays, middle- and low-latitude positive H bays, a partial recovery in Sym-H, and the onset of Pi2 ULF pulsations. In addition, we show that the auroral distribution develops in a systematic way during each cycle of a sawtooth substorm event. Specifically, a localized auroral onset develops on the lower branch of a thinned double-oval distribution. The location of onset is typically premidnight and often occurs to the west of intense omega band forms. This is followed by westward, eastward, and poleward expansion and the copious production of auroral streamers which can develop in complex patterns including a “spoke-like” morphology. The double-oval configuration thins again during the stretching phase until the next onset occurs and the cycle repeats. A schematic representation of the auroral dynamics associated with sawtooth substorms is also presented.

Citation: Henderson, M. G., et al. (2006), Substorms during the 10–11 August 2000 sawtooth event, *J. Geophys. Res.*, *111*, A06206, doi:10.1029/2005JA011366.

1. Introduction

[2] Magnetospheric sawtooth events were first identified in the LANL geosynchronous particle data by *Belian et al.* [1995] as large-amplitude, quasiperiodic (i.e., not strictly periodic) oscillations of the energetic particle fluxes. The oscillations are particularly prominent in the energetic proton channels, they typically occur during storm intervals in the presence of an enhanced ring current, they have a quasiperiodicity of approximately 2–4 hours, and they tend to be driven by moderate to strong ($B_z \approx -10$ nT) and continuously southward IMF conditions [e.g., see *Henderson*, 2004; *Henderson et al.*, 2006; J. E. Borovksy et al., The solar-wind driving of global sawtooth oscillations and periodic substorms: What determines the periodicity?,

---

[1] Los Alamos National Laboratory, Los Alamos, New Mexico, USA.
[2] Department of Physics and Astronomy, University of Calgary, Calgary, Alberta, Canada.
[3] Now at Solar-Terrestrial Physics Group, School of Physics and Astronomy, University of Southampton, Southampton SO17 1BJ, UK.
[4] Space Environment Center, NOAA, Boulder, Colorado, USA.
[5] Department of Earth and Space Sciences, University of California, Los Angeles, California, USA.
[6] Space Sciences Laboratory, University of California, Berkeley, California, USA.
[7] NASA Goddard Space Flight Center, Greenbelt, Maryland, USA.
[8] Department of Physics and Astronomy, University of Iowa, Iowa City, Iowa, USA.

0148-0227/06/2005JA011366$09.00

submitted of *Annals of Geophysics*, 2005, hereinafter referred to as Borovsky et al., submitted manuscript, 2005]. They are called ‘‘sawtooth’’ events because the flux versus time profiles (rapid increases followed by more gradual decreases) resemble the teeth on a saw blade.

[3] The rapid flux increases and gradual decreases are associated with dipolarization and stretching at geosynchronous orbit and while this activity is typically strongest on the nightside (especially in the dusk-to-midnight sector), it can extend past the terminators into the dayside (Borovksy et al., submitted manuscript, 2005). In addition, *Henderson* [2004] showed that the strong nightside stretching and dipolarization can also extend well inside of geosynchronous orbit. Each tooth in a sawtooth event is also usually associated with a partial recovery of the Sym-H index [*Reeves et al.*, 2003; *Huang et al.*, 2004a; *Henderson*, 2004; *Henderson et al.*, 2006]; energetic particle injections [*Reeves et al.*, 2003; *Huang et al.*, 2003a; *Henderson*, 2004; *Henderson et al.*, 2006]; enhancements of energetic neutral atom (ENA) emissions [*Reeves et al.*, 2003; *Huang et al.*, 2003a; *Henderson et al.*, 2006]; pulses of low-charge-state (i.e., ionospheric origin) energetic oxygen [*Henderson et al.*, 2006]; tail signatures of TCRs and plasmoids [*Huang*, 2002; *Huang et al.*, 2003b; *Lui et al.*, 2004]; localized auroral onsets in the premidnight sector [*Reeves et al.*, 2003; *Henderson et al.*, 2006] which occur on the lower branch of a thinned down double-oval configuration [*Henderson et al.*, 2006]; auroral zone negative H bays [*Huang et al.*, 2003a]; middle- and low-latitude positive H bays [*Huang et al.*, 2004a]; Pi2 pulsations with substorm-like polarizations signatures [*Kitamura et al.*, 2005]; and unusually wide substorm-like current wedges [*Kitamura et al.*, 2005].

[4] At present there is still some debate as to whether sawtooth events are sequences of quasiperiodic substorms or some different type of global disturbance. Although Borovksy et al. (submitted manuscript, 2005) describe the individual teeth as substorm-like, they distinguish them from isolated or periodic substorms because they tend to produce disturbances that are more azimuthally distributed than one might expect from typical substorms. In addition, *Lee et al.* [2004] and *Lee and Lyons* [2004] contend that many of the observational features present during sawtooth events are not consistent with substorm behavior, but rather are global disturbances directly driven by SW (Solar Wind) pressure enhancements. Although *Lee et al.* [2004] acknowledged that substorm effects could also be present during the teeth, they suggested that the dominant magnetospheric response is due to a global pressure effect and they explicitly attribute many of the observational features that one would normally associate with substorm activity to this pressure effect. In more recent studies, *Lee et al.* [2005] and *Lyons et al.* [2005] conclude that teeth can either be substorms or that they are composed of a two-mode response: a global pressure effect and in some cases a substorm effect. However, *Lyons et al.* [2005] still explicitly attributes to pressure effects, observational characteristics that have long been associated with substorm effects instead. Other studies [*Reeves et al.*, 2003; *Huang*, 2002; *Huang et al.*, 2003b; *Henderson*, 2004; *Lui et al.*, 2004; *Henderson et al.*, 2006; *Clauer et al.*, 2006] have concluded that sawtooth events are primarily storm time substorms. It is also important to note that others have examined sawtooth intervals as substorms in the past, before the term ‘‘sawtooth event’’ was coined. For example, the CDAW-9C event analyzed by *Pulkkinen et al.* [1991] and *Baker et al.* [1993] was considered to be a substorm, and the broader CDAW-9C interval (3 May 1986) was analyzed by *Minenko et al.* [2000a, 2000b] as a ‘‘chain of recurrent substorms.’’ However, as shown by *Henderson* [2004], this interval was also a sawtooth event.

[5] In large part, the notion that sawtooth events may constitute a new, previously unknown, mode of magnetospheric behavior may be rooted in a number of unsubstantiated assumptions, perhaps the most egregious of which is that sawtooth events produce simultaneous, globally dispersionless energetic particle increases at geosynchronous orbit. For example, *Lee et al.* [2004, paragraph 1] studied four sawtooth events and claimed that ‘‘during all four events, nearly simultaneous energetic particle flux enhancements and magnetic field variations occurred at all MLTs for each sawtooth cycle.’’ Furthermore, Borovksy et al. (submitted manuscript, 2005) claim that ‘‘with multiple satellites at geosynchronous orbit, the oscillations are seen nearly simultaneously and in-phase at all local times.’’ In addition, links have been made between non-substorm-like pressure-driven global auroral disturbances and sawtooth-like behavior [e.g., see *Lee and Lyons*, 2004, paragraph 32]. (Although we note that in a more recent study, *Lyons et al.* [2005] distinguish between pressure-driven teeth and substorm-associated teeth). The low- and middle-latitude positive H bays associated with many individual teeth have also been described as globally simultaneous and therefore not substorm-like [e.g., *Lee and Lyons*, 2003].

[6] Since sawtooth events typically last for several hours to a day, plots showing data acquired over an entire event (i.e., plots showing many hours of data) certainly seem to give the impression that each tooth is a globally simultaneous disturbance. However, as shown by *Henderson et al.* [2006], more detailed examinations of individual teeth show that the assumption of global simultaneity is typically not valid (although the disturbances associated with some sawtooth events can in fact be quite broad). In addition, since sawtooth events usually occur during anomalously high levels of solar wind driving (e.g., during solar wind magnetic cloud events), it is important to recognize that the magnetospheric response may be composed of more than one type of disturbance. For example, although solar wind shocks typically induce a different type of magnetospheric response than substorms do, both types of disturbances may be present in a single sawtooth interval. In this paper, we examine each of the individual teeth contained in the 10–11 August 2000 sawtooth event in detail in order to more clearly elucidate the nature of the underlying disturbances.

2. Observations

2.1. Geosynchronous and Auroral Behavior

[7] Los Alamos National Laboratory (LANL) SOPA energetic electron and proton spin-averaged differential flux measurements from three different locations around the Earth are presented in Figures 1a and 1b, respectively. The time interval shown extends for thirty hours from 1800 UT on 10 August 2000 to 2400 UT on 11 August 2000. For the electron channels shown in Figure 1a, the energy passbands are (from red to blue): 50–75 keV, 75–

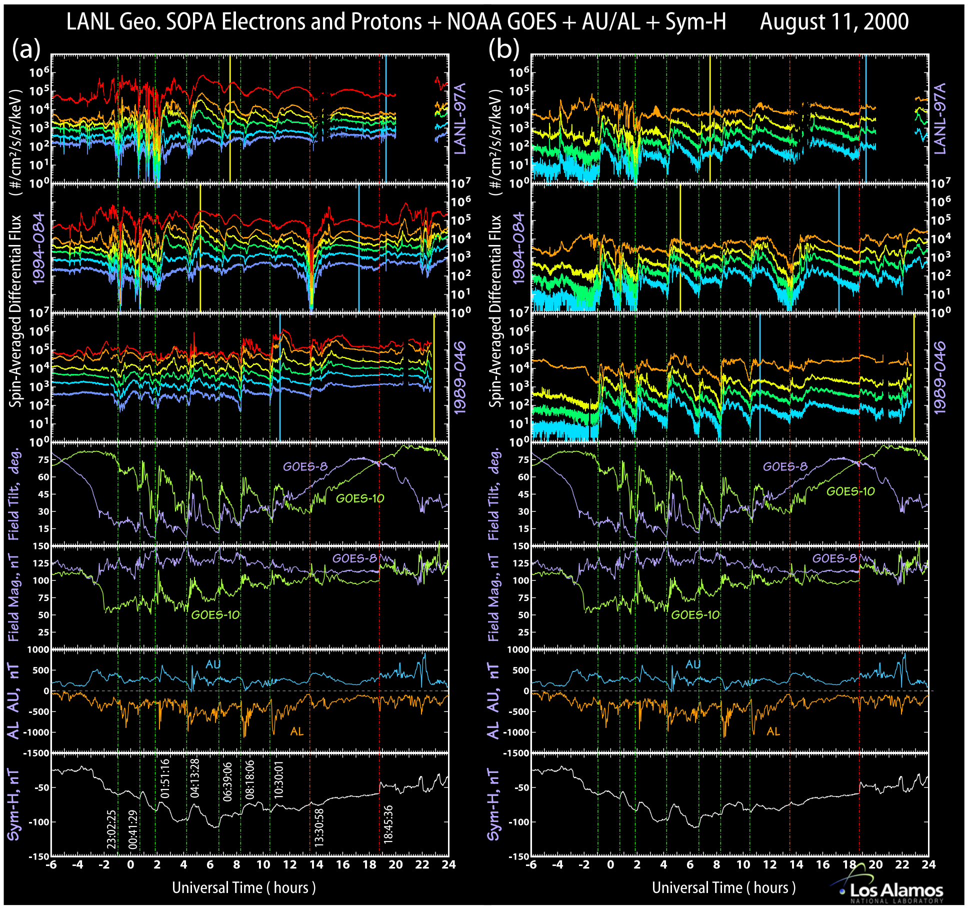

Figure 1. Los Alamos National Laboratory (LANL) energetic electron and proton data from three geosynchronous spacecraft stationed at various locations around the world together with field inclination angles at the GOES 8 and GOES 10 geosynchronous spacecraft, field magnitude at GOES 8 and GOES 10, AU and AL indices, and 1 min resolution Sym-H index. (a) Electrons with energies (from red to blue) 50–75 keV, 75–105 keV, 105–150 keV, 150–225 keV, 225–315 keV, 315–500 keV. (b) Protons with energies 75–113 keV, 113–170 keV, 170–250 keV, 250–400 keV. The vertical yellow and blue lines mark the time at which each satellite passed through local magnetic noon and midnight, respectively. Vertical dashed lines mark the onset of each "event" and are drawn at times 2302:25 UT (10 August), 0041:29 UT, 0151:16 UT, 0413:28 UT, 0639:06 UT, 0818:06 UT, 1030:01 UT, 1330:58 UT, and 1845:36 UT.

105 keV, 105–150 keV, 150–225 keV, 225–315keV, 315–500 keV. For the proton channels shown in Figure 1b, the energy passbands are (from orange to cyan) 75–113 keV, 113–170 keV, 170–250 keV, and 250–400 keV. Higher-energy channels (to several MeV) are available from the SOPA and ESP instruments and lower energy channels (extending from a few eV to about 40 keV) are available from the MPA plasma analyzer (and these will be described later). Also shown in Figure 1 are the field inclination angle at GOES 8 (purple) and GOES 10 (green), the field magnitude at GOES 8 (purple) and GOES 10 (green), the AU (blue) and AL (orange) indices, and the 1 min resolution Sym-H index. Data from GOES 11 (which was situated between GOES 10 and GOES 8 during this time period) are also available for this event and will be described later.

[8] The vertical dashed lines in Figure 1 mark the onset time of each sawtooth disturbance as indicated by a variety of different measures (not just the LANL geosynchronous data). Later, when we examine each tooth in more detail, we will discuss how each time was determined. For now, we note that each time line clearly marks the onset of a large-scale disturbance that is seen in most or all of the curves shown in Figure 1. For each of the events, a sharp sawtooth-like increase in the SOPA energetic proton fluxes is observed. Flux increases in the energetic electrons are also observed in association with most of the events, but they are not as dramatic (or as sawtooth-like) as the proton increases.

[9] The B field tilt angle at GOES 8 and GOES 10 plotted in Figure 1 is the angle between the magnetic field vector and the geocentric solar magnetospheric (GSM) equatorial plane (i.e., the $x-y$ axis). Thus an angle of 90° indicates that the field direction is perpendicular to the GSM equatorial plane (i.e., dipole-like), while low angles indicate a more tail-like stretched configuration. Differences in the behavior and magnitude of the variations between the two GOES spacecraft can be attributed to the fact that they are at different magnetic latitudes and at different local times. From Figure 1 we can see that all but the 2302:25 UT and

1845:36 UT events were associated with a substantial field dipolarization at one or more of the GOES spacecraft. For the 2302:25 UT and 1845:36 UT events, all of the GOES spacecraft were situated on the dayside and for the 1330:01 UT event, GOES 8 was situated on the dayside. Thus, for each event, a dipolarization was observed at a GOES satellite whenever it was situated on the nightside. In addition, the magnitude of the dipolarizations tend to be very strong when the GOES spacecraft observed them in the premidnight sector and tend to be weaker when the spacecraft are away from that region.

[10] For all of the events, a substantial increase in the magnitude of the geosynchronous magnetic field was also observed. For most of the events, the B field increases in a pulse-like manner and appears to recover on a timescale substantially shorter than the intertooth period (of 2–4 hours). However, the B field increase associated with the 1845:36 UT event behaves differently in this regard. For this last event, the B field appears to increase much more promptly, and as a level shift rather than as a pulse.

[11] The auroral electrojet indices shown in Figure 1 reveal that most of the events were associated with a negative deflection in AL. Perturbations were also seen in AU for a number of the events, but their behavior is far less systematic than the AL response. In addition, the AL response for the 1845:36 UT event was an extremely sharp and short-lived negative pulse unlike the more substorm-like negative bays associated with the other events. The 0041:29 UT event was also not associated with an obvious negative bay in the AL index (but as we shall see this may have been due to limitations in station coverage).

[12] The bottom panel of Figures 1a and 1b shows that most of the events were also associated with a partial recovery in the Sym-H index. The one exception was the 1330:01 UT event which showed a small strengthening of Sym-H. Note that the evolution of the tooth-associated perturbations in Sym-H are very similar to the field magnitude increases seen at the GOES spacecraft. In particular, the perturbations tend to be pulse-like for all except the 1845:36 UT event which shows a very abrupt step-like increase in Sym-H.

[13] As pointed out recently by *Henderson et al.* [2006], the dramatic quasiperiodic oscillatory nature of sawtooth events is most easily seen in plots with time axes that span many hours because at least 2–3 teeth (i.e., at least 4–12 hours of data) are usually required to notice the sawtooth character. For example, the sawtooth behavior of the geosynchronous energetic proton fluxes for the 10–11 August 2000 event described here is very clear in the 30 hour plot shown in Figure 1. Note, however, that on such a long timescale, many of the teeth appear to represent dipolarization-associated dispersionless flux increases that occur simultaneously at all locations around the Earth and it is tempting to conclude that the individual teeth represent simultaneously global disturbances. For example, in a recent study, *Lee and Lyons* [2004] contend that, for the 10–11 August 2000 sawtooth event, there was a simultaneous occurrence of nightside magnetic variations and dayside particle flux changes. Other studies have also alleged the simultaneity of each tooth-related disturbance [e.g., *Lee et al.*, 2004; Borovksy et al., submitted manuscript, 2005] and there appears to be a general impression in the community that such simultaneity is a robust characteristic of sawtooth events. Nevertheless, we have found that more detailed analyses of sawtooth intervals usually reveals that the disturbances are typically not global nor simultaneous in nature. This was recently demonstrated for a specific case by *Henderson et al.* [2006].

[14] It has also been claimed that the geosynchronous energetic electron data “show very similar flux oscillations” to the proton data [e.g., *Lee et al.*, 2004]. However, as shown by *Henderson et al.* [2006], this was not at all true for the 18 April 2002 sawtooth event, and *Lee et al.* [2005] have demonstrated that substantial differences can indeed exist between the electron and proton flux profiles. In addition, even in the 30 hour plot shown in Figure 1, electron dispersion is quite apparent for the 10–11 August 2000 event discussed here.

[15] A further source of potential confusion also exists which has not been adequately addressed in previous studies of sawtooth events, and that is that the SOPA P1, P6, and (often) the P2 channels respond to electrons and can become severely contaminated by medium energy electrons when their fluxes are high. Ignoring this feature of the LANL SOPA instrument can lead to an incorrect characterization of the electron versus proton flux increases. Although we have omitted the the SOPA proton P1 and P6 channels in this section, the P2 channel has been retained in most plots. However, one should be wary of features in this channel that appear to be well correlated with the electron fluxes (or seem markedly uncorrelated with the adjacent P3-P5 channels) and in some plots (to follow) we have omitted the P2 channel altogether.

[16] In order to clarify the behavior of the geosynchronous energetic particle flux increases and their association with geosynchronous field dipolarizations and auroral activations for the 10–11 August 2000 event, we turn now to a more detailed examination of each tooth. In the following subsections, we present the LANL geosynchronous energetic electron and proton data over a 3 hour time window surrounding the onset of each flux increase. In addition, the GOES 10, GOES 11 and GOES 8 magnetic field tilt angle (or field magnitude) increases are shown together with global auroral imaging data from Polar/VIS or IMAGE/FUV when available. To further aid in the interpretation of the LANL SOPA energetic particle data, in Table 1 we have tabulated the drift times (gradient and curvature) for the upper energy threshold (i.e., fast particles) in each of the proton and electron energy channels. We used the approximate relativistic formula for a dipole given by *Hess* [1968],

$$\tau_D = \frac{163.77}{\eta}\left(\frac{m_e}{m}\right)\left(\frac{1+\eta}{2+\eta}\right)\frac{F(\lambda)}{L}, \text{minutes} \tag{1}$$

where η is the ratio of the particle’s kinetic energy to its rest energy, m_e is the electron rest mass, m is the particle rest mass, L is the L shell parameter, and $F(\lambda)$ is a pitch-angle-dependent quantity ranging between 1.0 (for equatorially mirroring particles) and 1.5 (for particles with a mirror latitude of 90°). Note that the relativistic corrections for protons in the SOPA energy range are very small because the proton rest energy is much larger ($E_\circ$ = 0.938 GeV). However, since the rest energy of an electron is only 0.511 MeV, relativistic corrections are significant over the

Table 1. LANL SOPA Energetic Particle Drift Times

SOPA Channel	Energy Range, keV	Comments	τ_D (24 MLT), min	$\tau_D/4$ (6 MLT), min
P1	50–75	usually bad	83.65	20.91
P2	75–113	often bad	55.52	13.88
P3	113–170		36.90	9.23
P4	170–250		25.10	6.27
P5	250–400		15.69	3.92
P6	400–670	usually bad	9.37	2.34
E1	50–75		89.36	22.34
E2	75–105		65.31	16.33
E3	105–150		47.17	11.79
E4	150–225		32.91	8.23
E5	225–315		24.61	6.15
E6	315–500		16.67	4.17
E7	500–750		11.90	2.98
E8	750–1100		8.66	2.16
E9	1100–1500		6.67	1.67

entire SOPA energy range. For example, 1 Mev electrons will drift slower than 1 MeV protons by a factor of about 1.5.

[17] For the IMAGE/FUV WIC data, each image is shown in Apex Magnetic Coordinates with noon at the top and midnight at the bottom. For the 1845:36 UT event, we have subtracted the airglow signal in order to more clearly see the entire global distribution (see *Immel et al.* [2000] for details on the airglow removal technique), but for all other events, the dayglow has not been subtracted. The latitude circles are drawn every 10° between 50° and 90°. For the Polar/VIS data, each image is presented in its raw format rather than a magnetic coordinate system.

2.1.1. The 2302:25 UT, 10 August Event

[18] An expanded 3 hour view of the LANL SOPA energetic electron and proton fluxes is presented in Figures 2c and 2d, respectively. The MLT locations of the three GOES spacecraft, the three LANL spacecraft, and the SAMNET/YORK ground station at 2302:25 UT are shown in Figure 2a. Note that the dots in Figure 2a are only meant to show the MLT of each observing point and are therefore drawn at arbitrary latitudes; that is, they should not be interpreted as magnetic footprint locations. As shown, at 2302:25 UT, GOES 10 and GOES 11 were in the postnoon sector and GOES 8 was situated just past the dusk terminator on the nightside. The 1989-046 spacecraft was situated near noon while the LANL-97A and 1994-084 satellites were situated in the predawn to dawn sector.

[19] One can immediately see from Figure 2d that the proton flux increases were not dispersionless at any of the

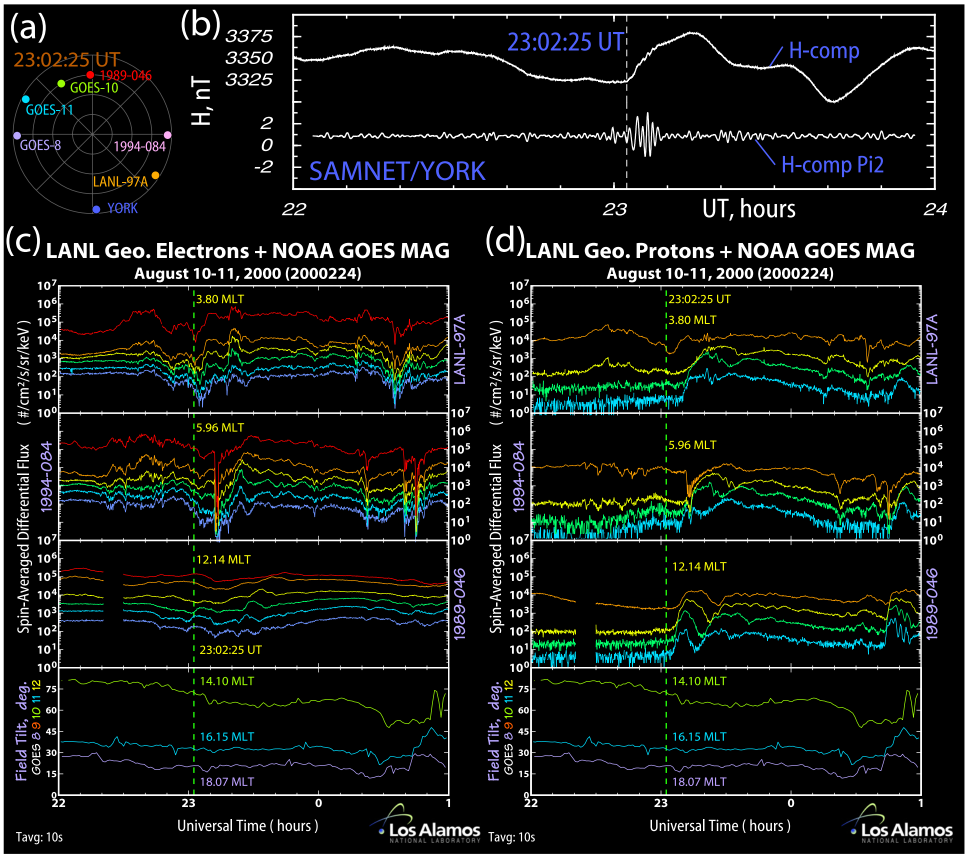

Figure 2. (a) Magnetic local time (MLT) positions of GOES 8, GOES 11, GOES 10, 1989-046, 1994-084, LANL-97A, and the York ground magnetometer station (the latitude is arbitrary). (b) One second resolution ground magnetometer data from York. The top trace is the unfiltered H component, while the lower trace is the Pi2-filtered (40–150 s) H component. (c and d) LANL geosynchronous energetic electron and proton data together with GOES 8, GOES 11, and GOES 10 field tilt angles for a 3 hour time period surrounding the 2302:25 UT (10 August) onset. The energies are the same as shown in Figure 1.

LANL spacecraft. In addition, none of the GOES spacecraft observed a dipolarization signature in association with this event. The onset time adopted for this event was therefore derived from the high-resolution, 1 s H component and Pi2-filtered H component traces from the SAMNET/YORK ground magnetometer station as shown in Figure 2b.

[20] From Figure 2d, we also note that the dispersion in the proton fluxes is least at 1989-046 and increases at 1994-084 and LANL-97A which were farther to the west. In addition, the electron flux increases appear to show the reverse behavior, with the most dispersion seen at 1989-046 and the least at LANL-97A. Although this behavior is consistent with an injection of energetic particles on the nightside, we must point out that both the electron and proton flux enhancements during this event were somewhat complicated and difficult to interpret. From the 1989-046 electron data, there is evidence that injection activity may have preceded the 2302:25 UT time and the LANL-97A and 1994-084 electron fluxes clearly show numerous fluctuations prior to the onset. In addition, the proton P2 channel at LANL-97A (top orange trace in Figure 2d) appears to show an apparently anomalous increase following the onset time. As we noted earlier, this is an artifact caused by electron contamination due to an increase in the electron fluxes at LANL-97A.

[21] Unfortunately, there was no global auroral imager data available from either Polar or IMAGE during this time period, so we cannot confirm that an auroral onset was also present, but from the data we do have, the event appears to be a substorm which was associated with an injection of energetic particles. From dispersion analysis, the western edge of the proton injection region could have been located as far west as 14–16 MLT.

2.1.2. The 0041:29 and 0151:16 UT, 11 August Events

[22] The second and third teeth are shown together in the same plot in Figure 3. During these teeth, the GOES spacecraft were moving into the nightside. All three observed dipolarizations with GOES 8 seeing it first. The dipolarization signature is delayed at GOES 11 and GOES 10 which are each farther to the west. The times for both events were derived from sharp increases in the GOES 8 dipolarization signatures.

[23] As can be seen from Figure 3c, the proton flux increases are dispersed with the least dispersion seen at 1989-046 and with the dispersion increasing as we move west to the 1994-084 and LANL-97A locations. Note that we have omitted the SOPA P2 channels from Figure 3c because they were contaminated near the onset times. As with the previous tooth, the electron flux increases are somewhat more complex than the proton flux increases and there are indications that some injection activity occurred before and after each of the nominal times marked by the vertical dashed lines. The electron signatures for the 0151 UT event show a dispersionless increase near dawn with progressively more dispersed signatures as you go east and this is consistent with a nightside substorm-associated injection event.

[24] No useful auroral images were available for the 0041 UT event, but Polar/VIS imagery was available for the 0151 UT event. Although the viewing geometry was quite poor, the images nevertheless show a substorm-like intensification progressing eastward from the premidnight sector. Note also, that the dawnside aurora does not activate simultaneously.

[25] Although the data available for these two events are less than perfect, it appears that they are consistent with being substorms.

2.1.3. The 0413:28 UT, 11 August Event

[26] By 0413:28 UT, all three of the GOES spacecraft were situated in the premidnight sector and they all saw very clear dipolarization signatures. The time of 0413:28 UT adopted for the onset of the event was obtained from sharp increases in the field tilt angle at GOES 8 and GOES 10. The dipolarizations for this event do not show any significant time delay between the three GOES spacecraft. At 0413:28 UT, the LANL/1989-046 spacecraft was situated a few hours to the west of GOES 10 on the dayside close to the dusk terminator. The energetic proton flux increases at 1989-046 is nearly dispersionless at the onset time (Figure 4c), but the energetic electron flux enhancements at 1989-046 are quite delayed relative to the onset time (Figure 4b). In addition, the proton arrival times become progressively more dispersed the farther west they are measured; that is, the proton flux enhancement is more dispersed at LANL-97A than it is at 1994-084. Note also, that this dispersive behavior is exactly reversed for the electrons; the least dispersed increase occurred at LANL-97A, and the dispersion progressively increases the farther east they are measured. This type of behavior is exactly what is expected from a substorm-associated nightside/duskside injection of energetic particles. In addition to these dispersed injection signatures, we note that numerous dispersionless flux variations were also observed throughout this event and were again likely due to external solar wind pressure variations.

[27] In addition to the excellent positioning of the three GOES spacecraft for this event, IMAGE/FUV also acquired excellent high-resolution images during the onset. A sequence of 15 images from the FUV/WIC instrument are shown in Figure 4a. The yellow box around the 0415:09 UT frame marks the first postonset image acquired by the WIC imager. The colored dots drawn on this image indicate the magnetic local times of the LANL and GOES spacecraft at 0415 UT (see Figure 4c for color-coding key and also note that the latitude of each dot is arbitrary here and should not be interpreted as the location of the magnetic footprint). Note that the image at 0415:09 UT, clearly shows the onset of an auroral substorm on the lower branch of a preexisting “double-oval” configuration. The auroral activity associated with this “embedded auroral substorm” is initially localized to the premidnight sector and subsequently expands poleward, westward and eastward. Such behavior is highly consistent with the Akasofu picture of an auroral substorm onset occurring in the equatorward portion of the discrete auroral emission region [*Akasofu*, 1964]. Furthermore, we note that while the onset is localized to the premidnight sector, there is also no obvious indication from the auroral measurements that any drastic dayside activations occurred immediately prior to the onset as has been suggested by others [*Lyons et al.*, 2005].

[28] We note that this tooth was also recently examined in some detail by *Lyons et al.* [2005] and *Lee et al.* [2005]. *Lee et al.* [2005] concluded that it was a “pressure driven” tooth that had a two-mode response consisting of a direct pressure

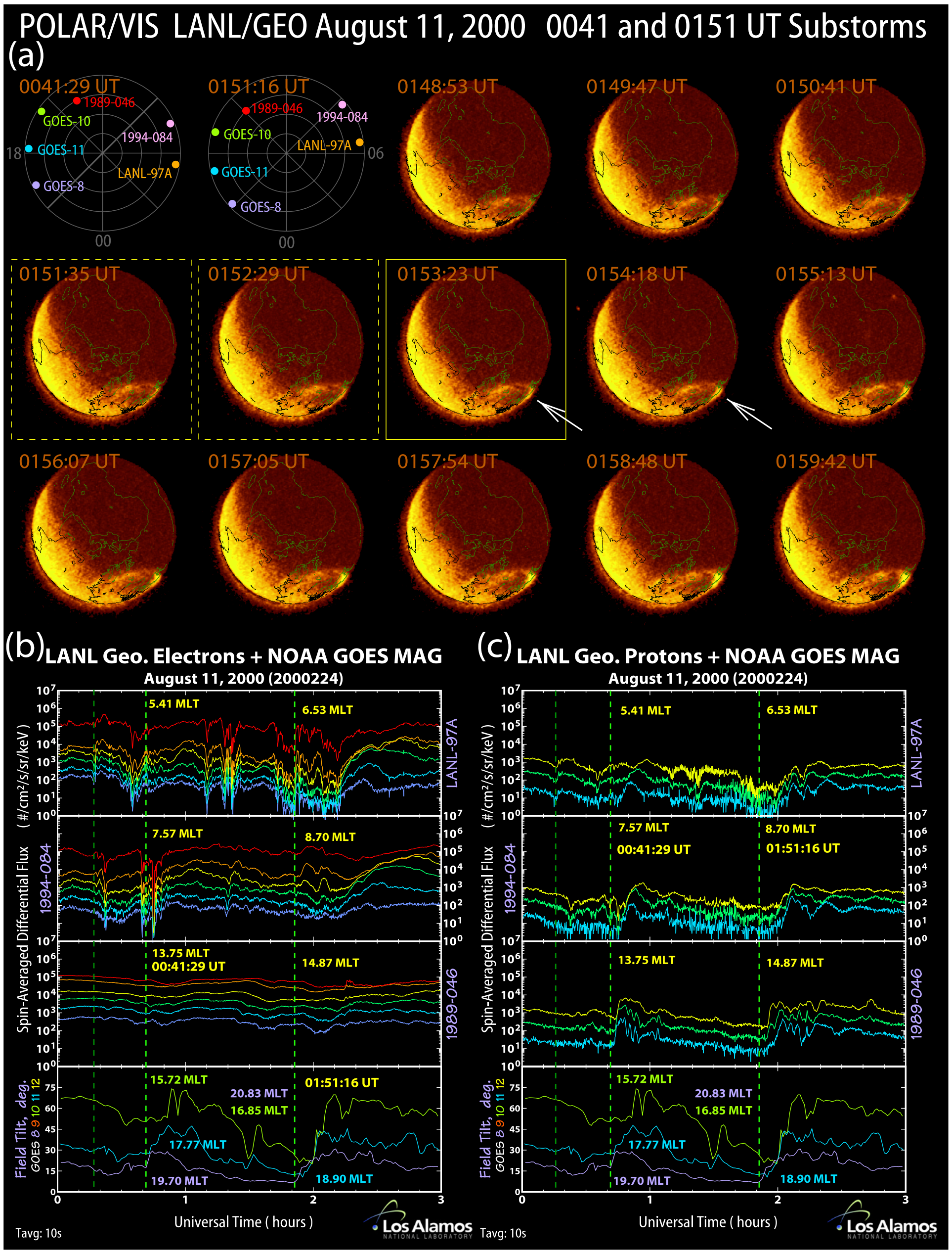

Figure 3. (a) Polar/VIS images illustrating the behavior of the auroral distribution around the time of the 0151 UT onset. (b and c) LANL geosynchronous energetic electron and proton data together with GOES 8, GOES 11, and GOES 10 field tilt angles for a 3 hour time period surrounding the 0151 UT onset. The energies are the same as shown in Figure 1. The MLT of each spacecraft at 0041:29 UT and 0151:16 UT is marked with a circle in the first two panels in Figure 3a (the latitude is arbitrary).

response combined with a substorm-like particle injection. *Lyons et al.* [2005] presented IMAGE/WIC data and concluded that the auroral emissions also displayed this two-mode type of response. However, from the auroral data presented in this section, we do not see a clear dayside auroral intensification just prior to the nightside onset as one might expect. Although the high-latitude feature near the dusk meridian and the lower-latitude emissions near dawn appear to intensify significantly following onset, we find that the high-latitude duskside form brightened at least 30 min prior to the tooth onset and was variable in both intensity and structure for entire period of time leading up to the tooth onset. This finding is in direct contradiction with the assertion by *Lyons et al.* [2005] that the feature brightened only in concert with the tooth onset and casts considerable doubt on the validity of the argument that its brightening is a visible indicator that the tooth behavior was to a great extent driven by a global pressure response. In addition, it is clear that by far the dominant auroral response during this tooth was a substorm-like onset and expansion starting in the premidnight sector. We will also explore this

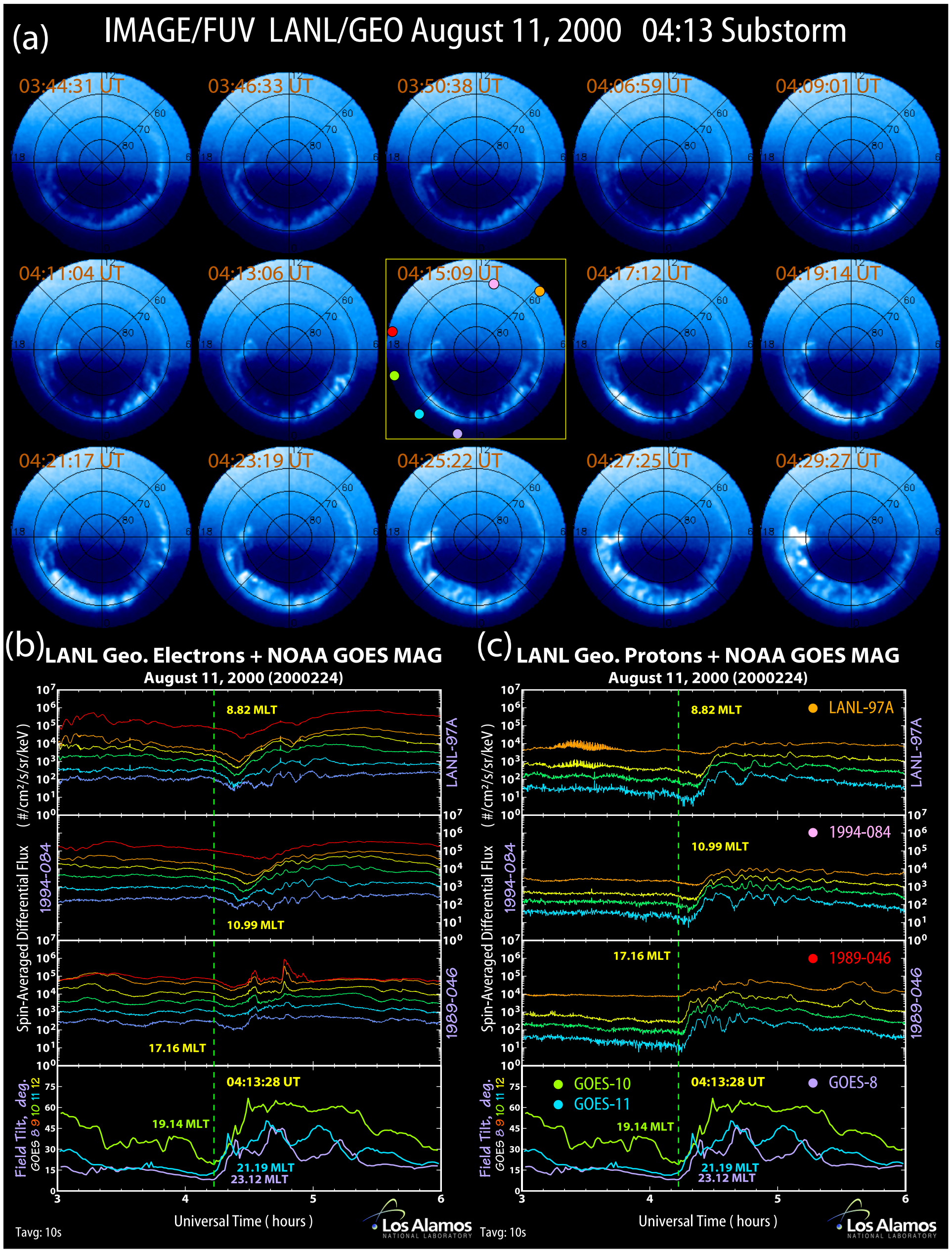

Figure 4. (a) IMAGE/FUV WIC images illustrating the behavior of the auroral distribution around the time of the 0413:28 UT onset. (b and c) LANL geosynchronous energetic electron and proton data together with GOES 8, GOES 11, and GOES 10 field tilt angles for a 3 hour time period surrounding the 0413:28 UT onset. The energies are the same as shown in Figure 1. The MLT of each spacecraft is marked with a circle on the 0415:09 UT image (the latitude is arbitrary).

behavior in more detail later in section 2.2 when we present auroral keograms of the IMAGE/WIC data.

[29] We further point out that *Lee et al.* [2005] attribute the near-dispersionless proton flux increase at 1989-046 together with the field dipolarizations at GOES 8 and GOES 10 as a "direct compression effect." Specifically, they state (paragraph 28) "that this proton flux enhancement at 17.3 MLT initiates nearly simultaneously with the initiation of the dipolarizations observed at 23.3 and 19.3 MLTs ... implies that this is the global direct response to the pressure pulse impact." Although we also find that there were significant (likely pressure related) dispersionless flux variations present in the LANL data during this tooth, we do not concur with *Lee et al.* [2005] that the existence of near-simultaneous dipolarizations at the GOES spacecraft and the near-dispersionless proton flux increase at 1989-046 necessarily imply that they were due to a direct pressure response. In our analysis of this event, we can see that not only is the data consistent with a broad injection region in the duskside/nightside, it is not consistent with a tailward propagating disturbance. From the field inclination angle inferred from the plasma data at 1994-084 and LANL-97A (data pre-

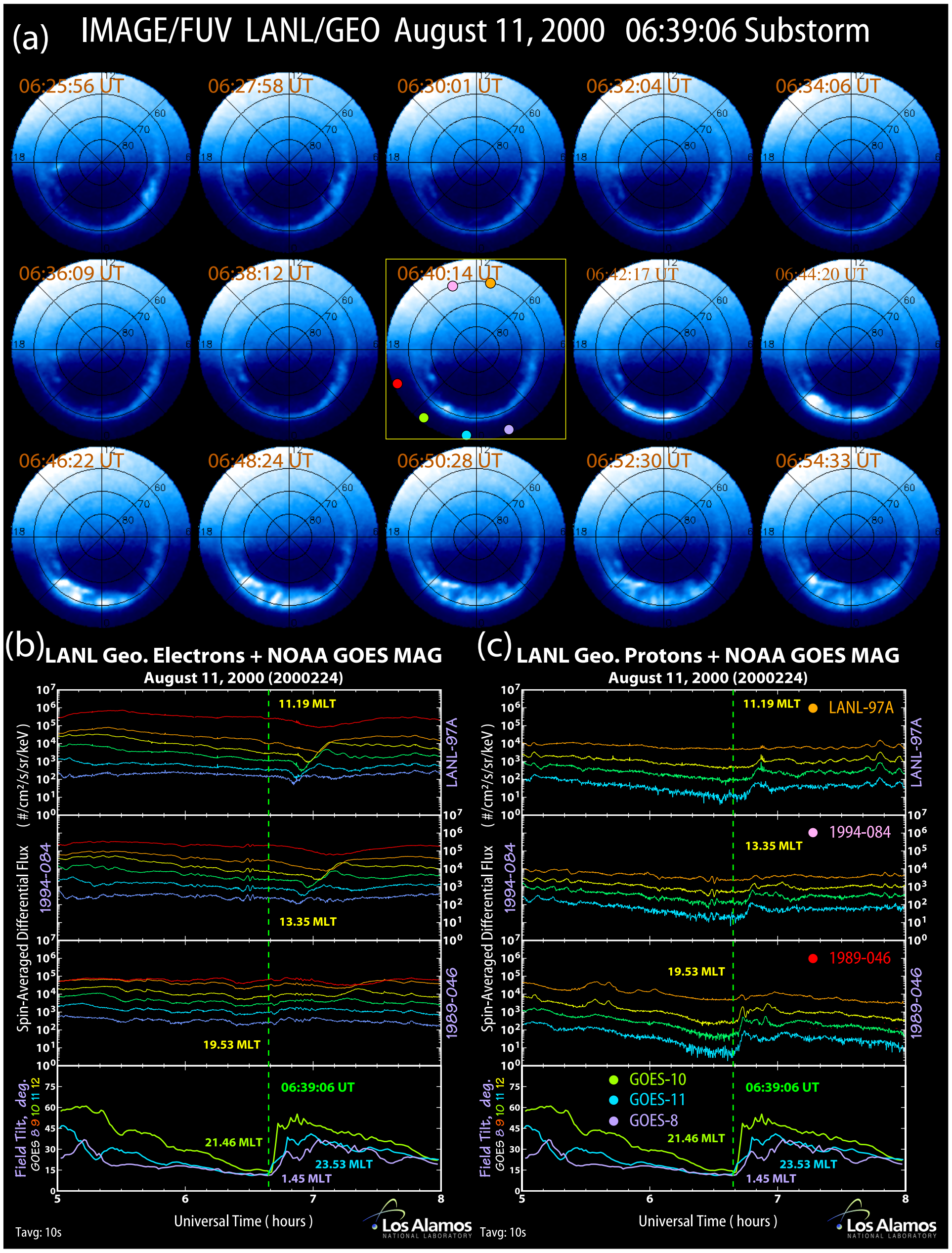

Figure 5. (a) IMAGE/FUV WIC images illustrating the behavior of the auroral distribution around the time of the 0639:06 UT onset. (b and c) LANL geosynchronous energetic electron and proton data together with GOES 8, GOES 11, and GOES 10 field tilt angles for a 3 hour time period surrounding the 0639:06 UT onset. The energies are the same as shown in Figure 1. The MLT of each spacecraft is marked with a circle on the 0640:14 UT image (the latitude is arbitrary).

sented later in section 2.4), we can see that there was no obvious disturbance on the dayside within several minutes of the onset time. However, there was a small increase in the angle substantially before onset, and it is possible that this was pressure induced. As well, the added data from the GOES 11 spacecraft indicates that the structure of the dipolarization on the nightside was not even locally the same.

2.1.4. The 0639:06 UT, 11 August Event

[30] For this tooth the three GOES spacecraft had moved farther to the east but were still very well situated in the premidnight to postmidnight sectors. All of the GOES spacecraft saw dipolarizations with only a small time delay between them. The dipolarization was seen first at GOES 11 at 0639 UT, and then about a minute or so later at GOES 10 (to the west) and GOES 8 (to the east). By 0639 UT, 1989-046 had also moved into the dusk-to-midnight sector and was situated at 19.53 MLT. As shown in Figure 5c, the proton flux increases at 1989-046 were sharp and only slightly dispersed. Furthermore, as with the previous tooth, the LANL satellites farther to the west show progressively more dispersed proton flux

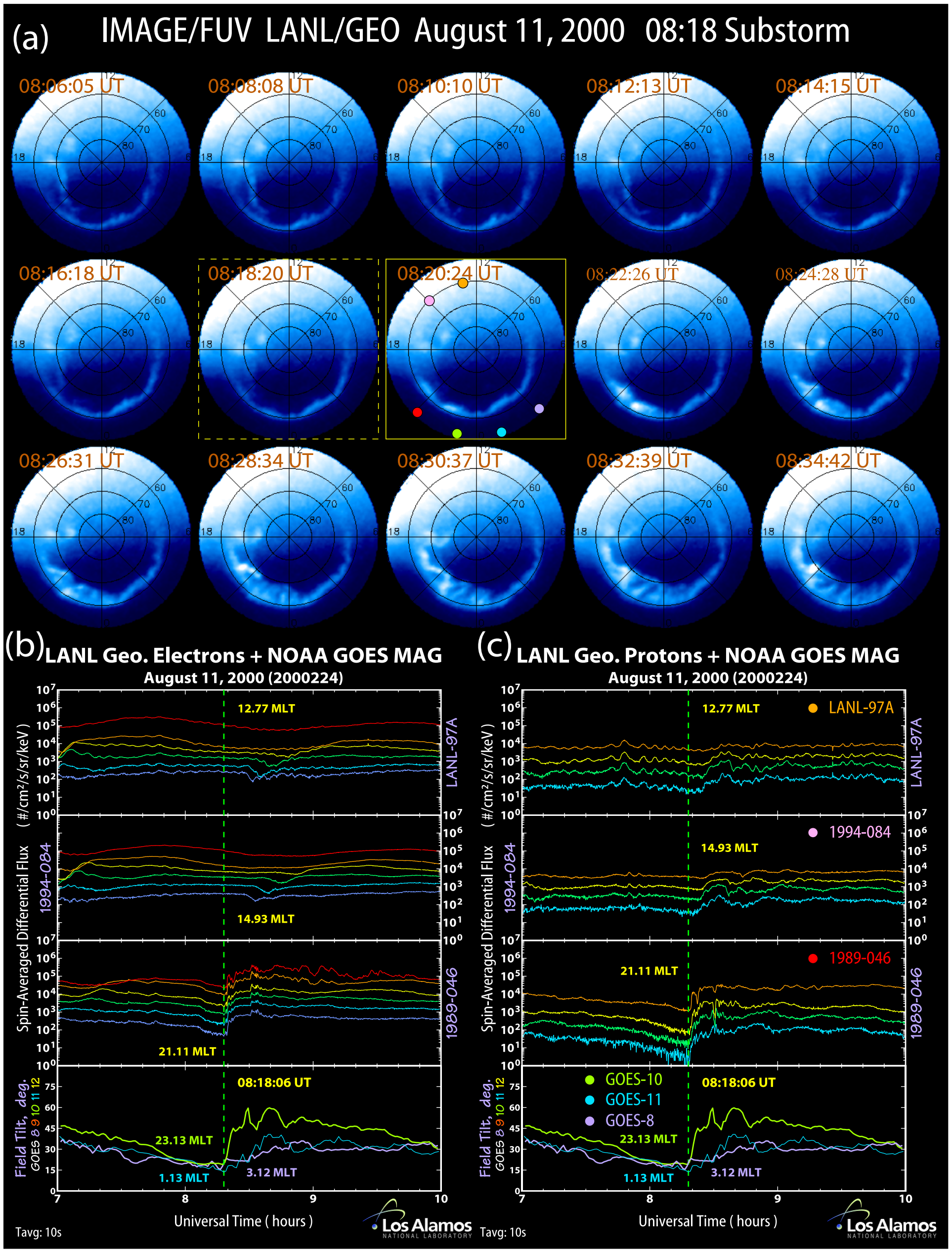

Figure 6. (a) IMAGE/FUV WIC images illustrating the behavior of the auroral distribution around the time of the 0818:06 UT onset. (b and c) LANL geosynchronous energetic electron and proton data together with GOES 8, GOES 11, and GOES 10 field tilt angles for a 3 hour time period surrounding the 0818 UT onset. The energies are the same as shown in Figure 1. The MLT of each spacecraft is marked with a circle on the 0820:24 UT image (the latitude is arbitrary).

increases. Meanwhile, the electron dispersion characteristics are exactly reversed, with the least dispersion seen at LANL-97A and the most seen at 1989-046 (see Figure 5b). As with the previous tooth, the observed electron and proton dispersion patterns are highly consistent with a classic nightside substorm-associated injection. The small amount of proton dispersion observed at 1989-046 indicates that it was very close to, but outside (westward) of the injection region during this event.

[31] Excellent IMAGE/FUV global auroral images are also available for this event and are shown in Figure 5a. As can be seen, a localized premidnight sector embedded substorm onset is clearly observed in the first postonset image acquired at 0640:14 UT (highlighted with a yellow frame). The postonset expansion phase activity during this tooth is also highly consistent with the Akasofu description of auroral substorm activity. In addition, we do not see any systematic onset-associated, simultaneously global activations of the aurora in Figure 5a.

[32] From the data presented here, it is clear that this event was a substorm, and we note that *Lyons et al.* [2005] arrived at the same conclusion.

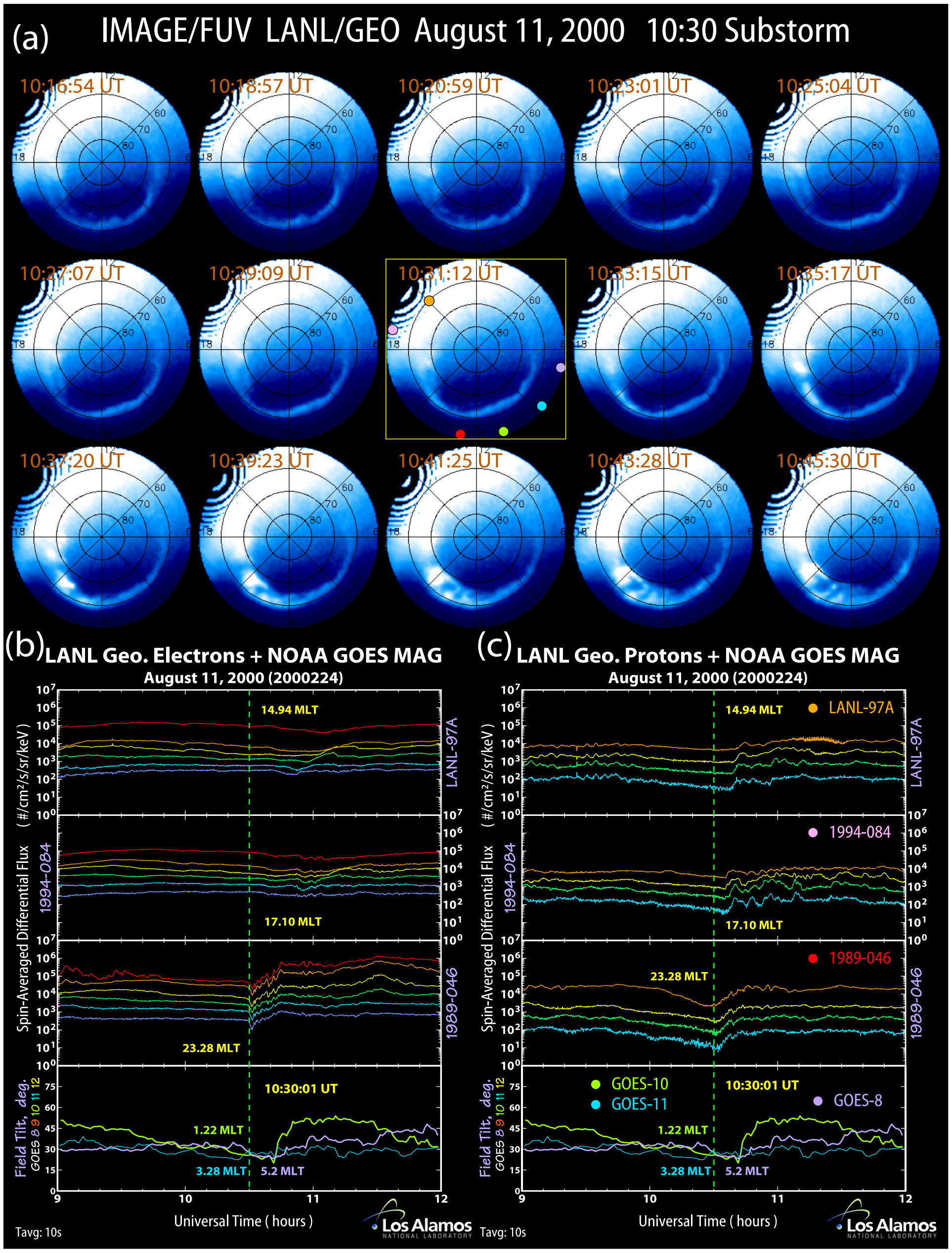

Figure 7. (a) IMAGE/FUV WIC images illustrating the behavior of the auroral distribution around the time of the 1030:01 UT onset. (b and c) LANL geosynchronous energetic electron and proton data together with GOES 8, GOES 11, and GOES 10 field tilt angles for a 3 hour time period surrounding the 1030:01 UT onset. The energies are the same as shown in Figure 1. The MLT of each spacecraft is marked with a circle on the 1031:12 UT image (the latitude is arbitrary).

2.1.5. The 0818:06 UT, 11 August Event

[33] For this tooth, GOES 10 was situated in the premidnight sector at 23.13 MLT, while GOES 11 and GOES 8 were situated in the postmidnight sector at 1.13 MLT and 3.12 MLT respectively. GOES 10 and GOES 11 both saw field dipolarizations, but GOES 10 was the only one that saw a very dramatic sharp dipolarization. The 0818:06 UT time adopted for this event was derived from the GOES 10 dipolarization. GOES 8, which was the easternmost of the GOES spacecraft did see a systematic postonset increase in the field inclination angle, but it was fairly gradual in comparison to what was observed at GOES 10 and GOES 11. At 0818:06 UT, 1989-046 was very well situated in the premidnight sector and as shown in Figures 6b and 6c, it observed abrupt dispersionless proton and electron flux increases in conjunction with the GOES 10 dipolarization. Proton dispersion increases toward the west while electron dispersion increases toward the east, which is, again, consistent with a nightside substorm injection.

[34] The IMAGE/FUV WIC data for this event (Figure 6a) also shows an embedded auroral onset associated with the dipolarization. Furthermore, although still

localized to the premidnight sector, the onset is somewhat wider in MLT range than the previous onsets and appears to show two adjacent regions activating at once. The initial onset region expands poleward, eastward and westward and is consistent with an Akasofu-type auroral substorm. We also note that aside from the substorm disturbance, there was no other global auroral activation associated with the tooth onset.

[35] From the data presented here, this tooth also appears to be a substorm, and we note that this is also in agreement with the findings of *Lyons et al.* [2005].

2.1.6. The 1030:01 UT, 11 August Event

[36] During this tooth, the three GOES spacecraft were all situated in the midnight-to-dawn sector. Of these spacecraft, GOES 10 (which is the westernmost of the trio), was the only one that observed a dramatic dipolarization signature. On the other hand, the LANL 1989-046 spacecraft was well situated in the premidnight sector and observed dispersionless flux increases in both electrons (Figure 7b) and protons (Figure 7c). Again, as with the previous teeth, the dispersion signatures are consistent with a nightside injection source. It is interesting to note, however, that the dipolarization signature observed at GOES 10 was significantly delayed relative to the particle enhancements at 1989-046. The time adopted for the onset of this tooth was obtained from 1 s resolution Pi2-filtered ground magnetic H component data from Bikia (BIK).

[37] IMAGE/FUV WIC global auroral images are also available for this tooth and are shown in Figure 7a. The first postonset image was acquired at 1031:12 UT and is marked with a yellow box. As can be seen, the onset was localized near the 21–22 MLT sector and subsequently expanded poleward, eastward and westward as is typical for auroral substorm expansion phase activity. We note that, as with the other teeth examined thus far, no global activations were seen at onset. Furthermore, the envelope of auroral activity in the substorm bulge region appears to take over 10 min to propagate into the postmidnight sector where the GOES 10 spacecraft was situated, and this may very well explain the relatively long time delay between the dispersionless injection at 1989-046 and the dipolarization signature at GOES 10. On the basis of the IMAGE/FUV data together with the LANL and GOES geosynchronous observations, this tooth also appears to be a substorm.

2.1.7. The 1330:58 UT, 11 August Event

[38] By the time this event occurred, the three GOES spacecraft had moved into the dawn sector and were not well situated to observe nightside field dipolarizations. At 1331 UT, GOES 10 was the only one of the three remaining on the nightside at 4.27 MLT. Neither GOES 11 nor GOES 8 observed any evidence of a dipolarization associated this event, but a small increase in the field inclination angle was observed at GOES 10 near 1333 UT (in passing, it is interesting to note how sharp this increase looks in the 30 hour plot shown in Figure 1). By 1331 UT, the LANL 1989-046 spacecraft had also moved into the postmidnight sector and LANL-97A and 1994-084 had entered into the dusk-to-midnight sector.

[39] The time adopted for the start of this event was 1330:58 UT and was determined from the 1 s resolution Pi2-filtered ground magnetometer H component trace from MacQuarie Island (MCQ) shown in Figure 8b. At 1330:58 UT, MacQuarie Island was located just past the midnight meridian as shown in the last panel of Figure 8a.

[40] At 1989-046, small dispersionless electron and proton flux increases were observed in conjunction with the field dipolarization at GOES 10. Also, at 1994-084, which was situated to the west of 1989-046, a slightly dispersed proton flux enhancement was observed while the electron fluxes displayed a dropout-like (probably lobe entry) behavior which was punctuated by a sudden pulse-like partial recovery followed by a step-like recovery. In addition, although LANL-97A had numerous data gaps after 1330 UT, the data that is available from that spacecraft shows that there was a very gradual nearly dispersionless increase in both the electron and proton fluxes associated with this event, although it was delayed relative to the more abrupt increase seen at 1989-046.

[41] Because of the poor locations of the GOES spacecraft, and the complexity of the LANL data, we cannot say with certainty from these data sets alone whether the 1330:58 UT event was associated with a substorm-like injection on the nightside. However, a secondary burst of Pi2 pulsations was observed at MacQuarie Island at 1410:20 UT as shown in Figure 8b. This Pi2 pulse appears to be associated with a dispersed electron population seen at 1989-046 (located to the east) and a dispersed proton population seen at 1994-084 (located to the west) and does appear to be consistent with a nightside injection of particles. In addition, from the 30 hour plot shown in Figure 1, it is clear that electron fluxes at LANL-97A and 1994-084 began increasing near ≈14 UT, much later than the increase seen at 1989-046. Thus it appears that a true injection did occur during this tooth.

[42] No IMAGE/FUV data was available during this event. Polar/VIS global auroral images of the southern polar cap are available and are shown in Figure 8a, but unfortunately, the last frame available was acquired several minutes before the 1330:58 UT onset time. We are therefore unable to determine whether an auroral onset was observed in association with either of the Pi2 bursts. The frames that are available show that the Southern Hemisphere auroral distribution displayed a prominent double-oval type configuration, which, as we have seen for the previous teeth, is a typical preonset configuration during sawtooth events.

2.1.8. The 1845:36 UT, 11 August Event

[43] At 1845 UT, the three GOES spacecraft were positioned symmetrically around the the noon meridian with GOES 11 at 11.83 MLT and GOES 10 and GOES 8 situated prenoon and postnoon at 9.77 MLT and 13.75 MLT respectively. 1989-046 was in the dawn to noon sector (at 7.80 MLT) and LANL-97A and 1994-084 were situated premidnight and postmidnight respectively (at 23.46 MLT and 1.62 MLT). A small dipolarization is observed at GOES 11 and GOES 8, but no clear dipolarization signature was observed at GOES 10 (data shown later in section 2.4). Nevertheless, as shown in Figures 9b and 9c, all three GOES spacecraft observed an abrupt and simultaneous increase in the B field magnitude. In addition, the proton flux increases observed at the three LANL spacecraft were globally dispersionless and virtually simultaneous (Figure 9c). This is also true for the electron flux increases, although we note that the electron fluxes increased by only a small amount (Figure 9b). The ground magnetometer data

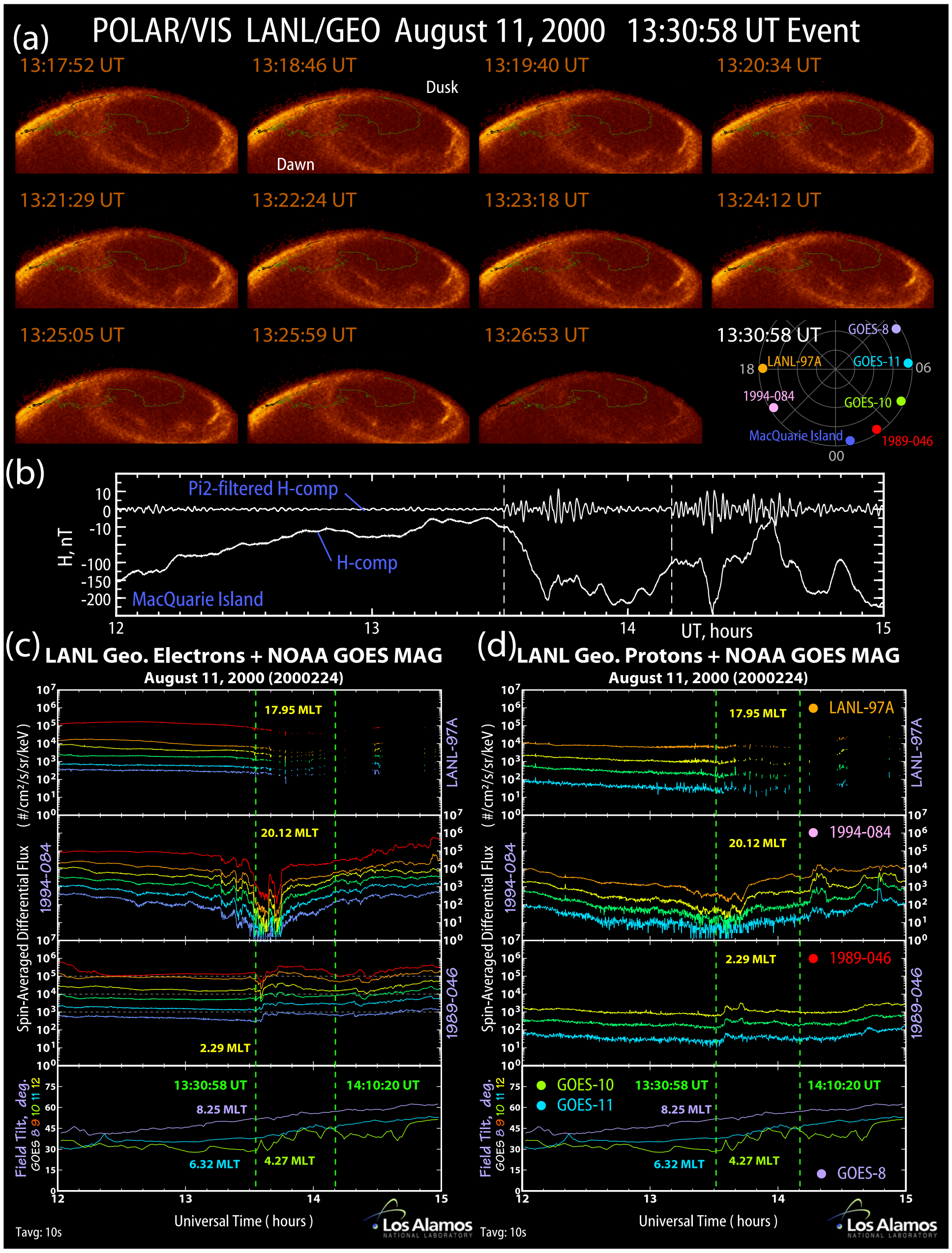

Figure 8. (a) Polar/VIS Southern Hemisphere images illustrating the behavior of the auroral distribution prior to the 1330:58 UT onset. Unfortunately, no images were acquired after 1326:53 UT. (b and c) LANL geosynchronous energetic electron and proton data together with GOES 8, GOES 11, and GOES 10 field tilt angles for a 3 hour time period surrounding the 1330:58 UT onset. The energies are the same as shown in Figure 1. The MLT of each spacecraft at 1330:58 UT is marked with a circle in the last panel in Figure 8a (the latitude is arbitrary).

also showed a global near-simultaneous abrupt increase and we adopted a time of 1845:36 UT based on 1s H component data from the SAMNET/YORK station.

[44] From Figures 9b and 9c, we can also see that there was no clear evidence of any drifting energetic electron or proton populations at geosynchronous orbit following the abrupt field increase. Thus, unlike the previous events, this one did not appear to be associated with a localized injection of energetic particles anywhere at geosynchronous orbit. Instead, the dispersionless flux enhancements were produced as a result of the spacecraft sampling different particle populations due to a rapid, global field reconfiguration. Furthermore, this is exactly what one would expect if the field increase were due to the arrival of an IMF/SW shock.

[45] Fortunately, IMAGE/FUV images were available during this event and are shown in Figure 9a. The first postflux increase image was taken at 1846:20 UT (marked with a yellow frame) and clearly shows an intensification of the high-latitude aurora in the postnoon sector. Interestingly,

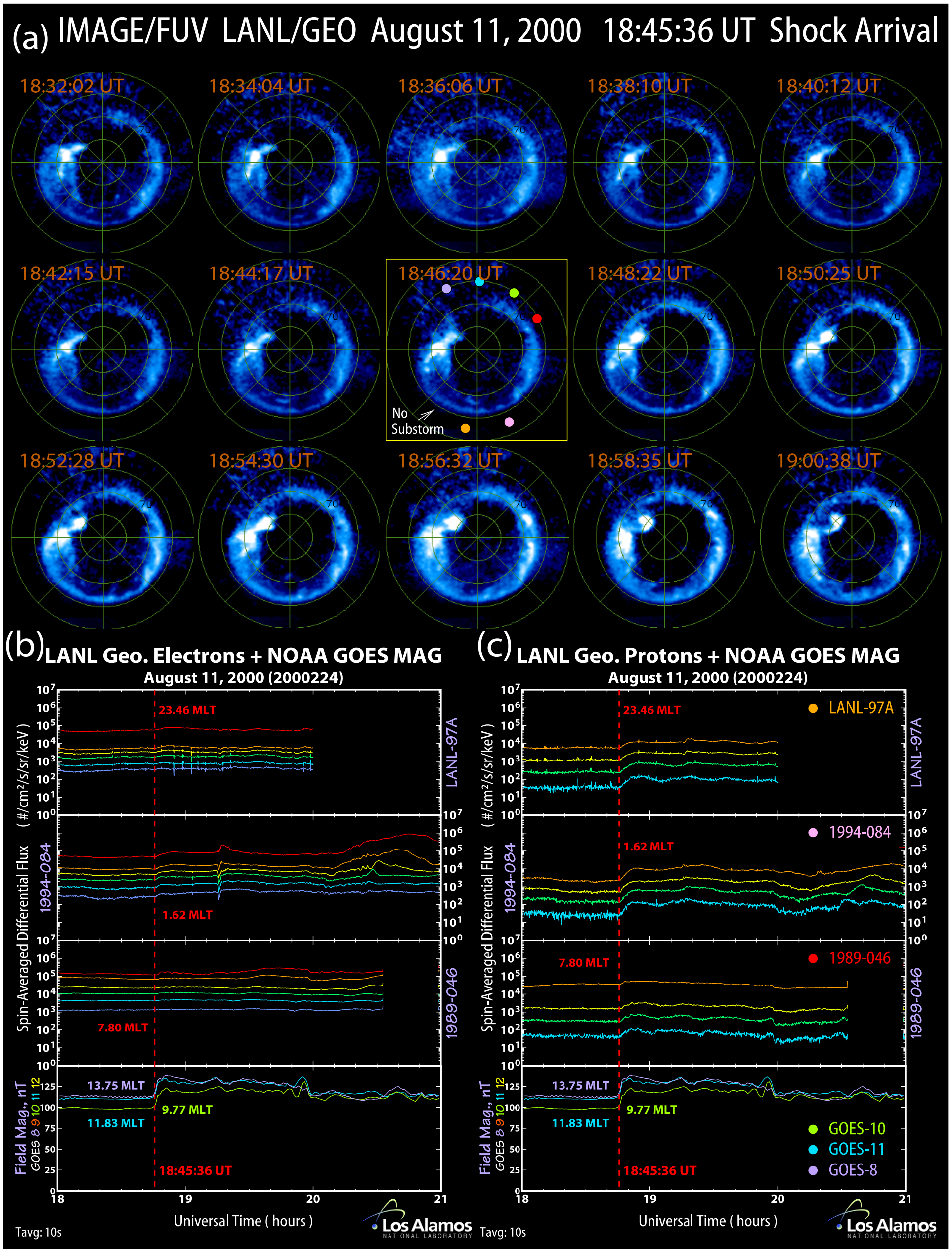

Figure 9. (a) IMAGE/FUV WIC images illustrating the behavior of the auroral distribution around the time of the 1845:36 UT dispersionless flux increase. (b and c) LANL geosynchronous energetic electron and proton data together with GOES 8, GOES 11, and GOES 10 field magnitudes for a 3 hour time period surrounding the 1845 UT event. The energies are the same as shown in Figure 1. The MLT of each spacecraft is marked with a circle on the 1846:20 UT image (the latitude is arbitrary).

however, there is no substorm onset observed on the nightside (or anywhere else) in this or in subsequent frames. The entire auroral distribution appears to become intensified following the B field increase (as expected), but there was no substorm associated with this activity. Instead, the most noticeable changes to the auroral distribution occurred in the high-latitude afternoon sector and consisted of an expansion and brightening of the aurora toward the pole.

[46] *Lee and Lyons* [2004] and *Lyons et al.* [2005] have also examined this event in detail. *Lyons et al.* [2005] classified it as a typical pressure driven global disturbance. Furthermore, *Lee and Lyons* [2004] also found that it was global and near simultaneous, but they also claimed that "On the basis of [nightside examples], we presume that the nightside magnetic response to the pressure pulse was dipolarization-like; however, this cannot be confirmed because of the absence of magnetic field measurements on the nightside." In contrast with this claim, from the data presented here, it can be seen very clearly that the 1845:36 UT event was not associated with a large-scale dipolarization-like event on the nightside. Clearly this event is both qualitatively and quantitatively different from the

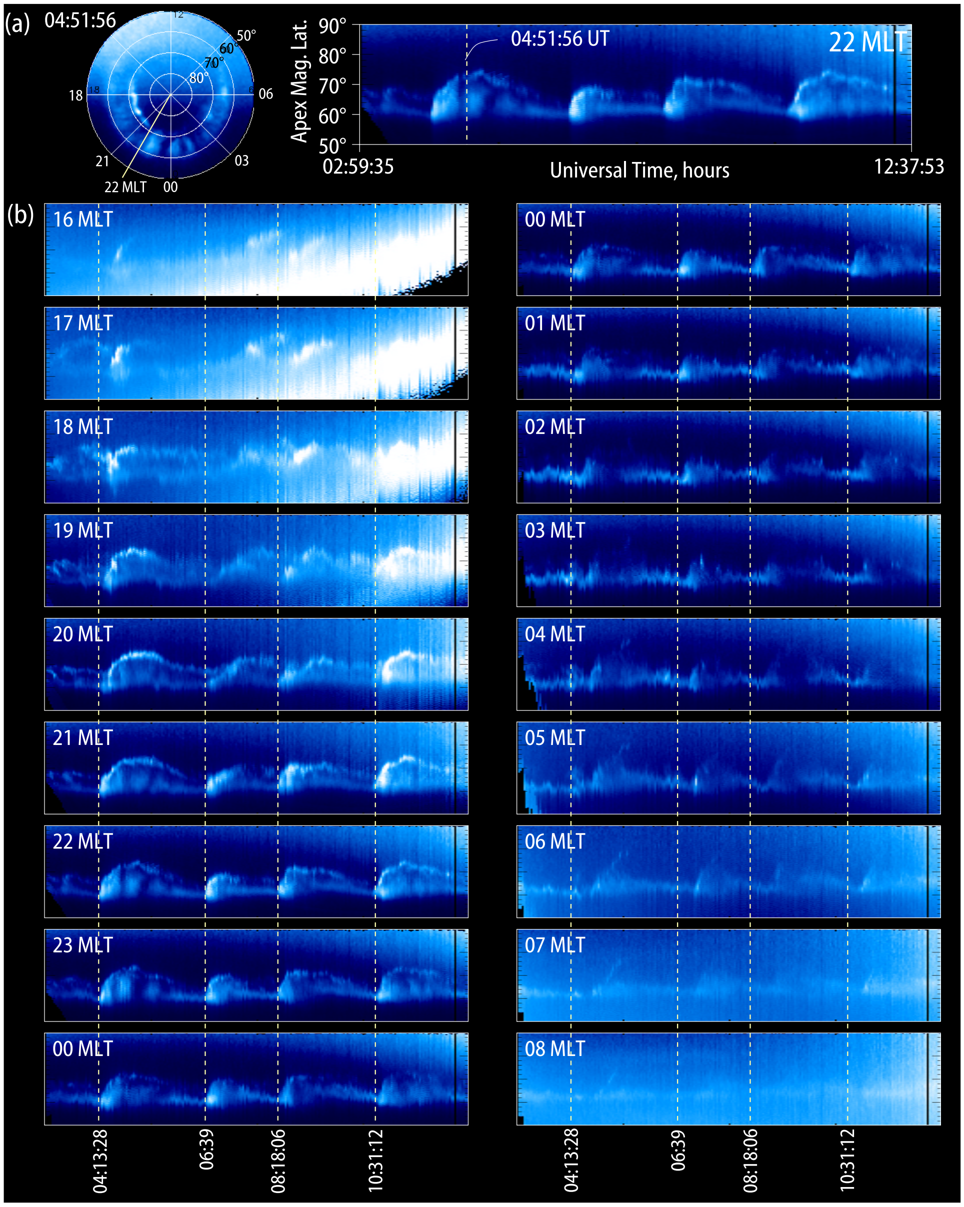

Figure 10. Keograms generated from a series IMAGE/FUV WIC images showing the latitudinal motion of the aurora. (a) An example showing how keograms are created. The auroral intensities along a given meridian is extracted from each image and stacked next to one another to create a latitude-versus-time plot. (b) Keograms for MLT meridians ranging from 16 MLT through midnight to 08 MLT.

earlier teeth. In fact, we would not have originally considered this event to be a tooth due to the lack of substantial electron flux enhancements and its obvious shock-associated appearance.

2.2. Synopsis of Auroral Behavior and IMAGE/FUV Keograms

[47] In Figures 4–7 we presented sequences of IMAGE/FUV WIC images illustrating the behavior of the northern auroral distribution before, during and after the onset of the 0413, 0639, 0818, and 1031 UT teeth. In each case, the onset of the tooth was associated with a localized brightening of the auroral distribution in the dusk to midnight sector on the lower branch of a "double-oval" configuration. A double-oval configuration is one in which a broadly extended (in azimuth) region of auroral emissions resides poleward of the main auroral oval. Such double-oval configurations are known to develop out of the recovery phase of some substorms and are also characteristic of steady magnetospheric convection (SMC) intervals.

[48] In each case, a double-oval configuration is observed during the time period leading up to onset, although in some cases the poleward portion is somewhat faint and hard to see in the individual images. The double-oval progressively thins until a localized onset occurs on the equatormost portion in the dusk to midnight sector. Then the initially localized brightening expands poleward, eastward and westward in a manner quite consistent with the Akasofu picture of auroral substorm development. This behavior was also found to occur in the 18 April 2002 sawtooth event

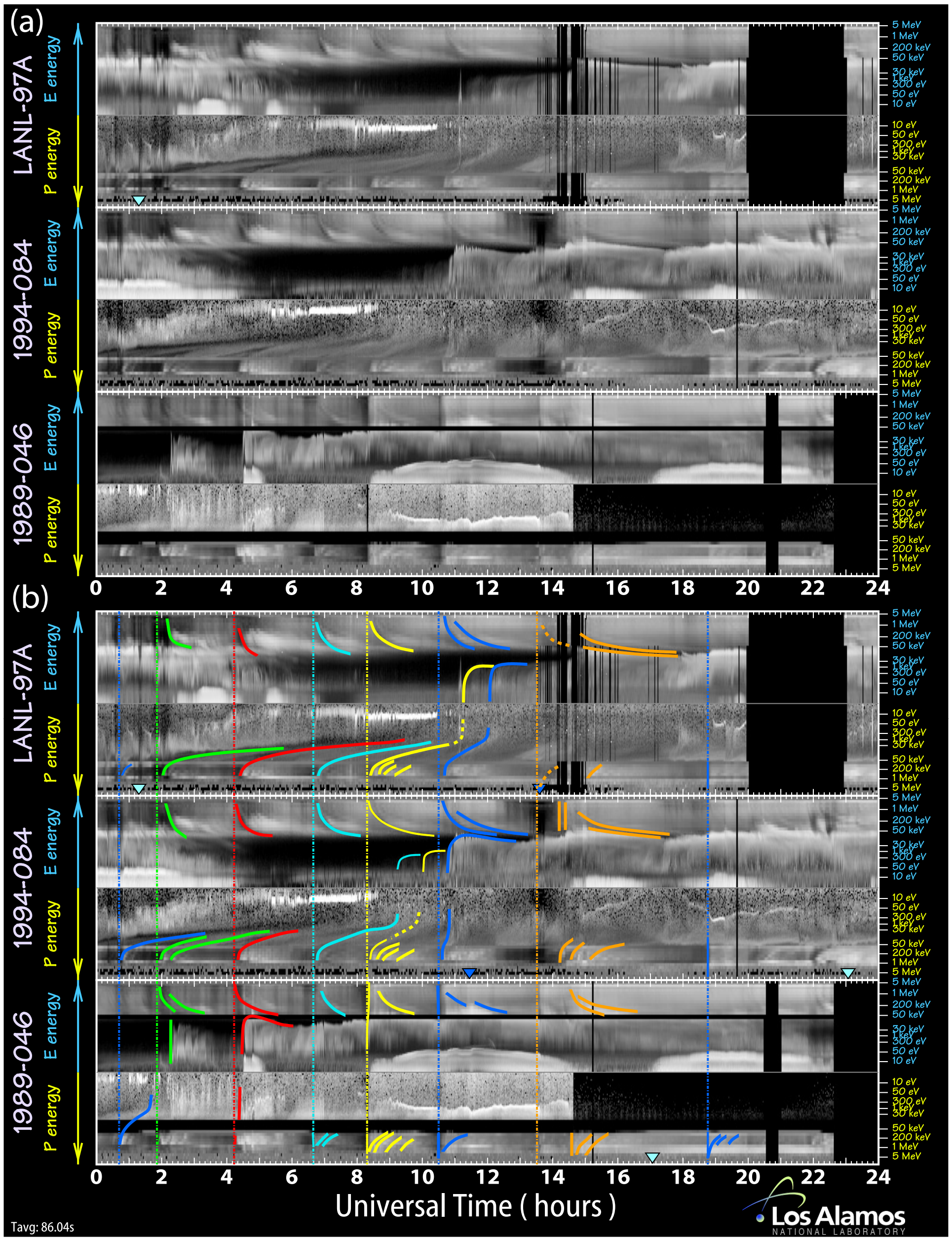

Figure 11. Energy versus time flux perturbation maps constructed by merging together data from three separate instruments on the LANL geosynchronous spacecraft (MPA, SOPA, and ESP). The protons are shown with an inverted energy scale.

[*Henderson et al.*, 2006] and appears to be fairly typical of sawtooth events in general.

[49] In Figure 10, we present an alternate way of viewing the temporal and spatial evolution of the auroral distribution. Shown are keograms constructed from the raw IMAGE/FUV WIC images at 17 different magnetic local times. For each panel, slices of the auroral intensity along the given MLT meridian are stacked next to one another in order to create latitude versus time plots. Figure 10a illustrates this process for the 22 MLT keogram. The behavior described above is clearly illustrated in this format. Specifically each onset occurs on the lower branch of a thinned down double-oval configuration. The envelope of auroral activity expands poleward and then develops into a new double-oval configuration which then thins down again prior to the next onset. By comparing keograms at different MLTs, it is also very clear that the auroral activity does not expand poleward simultaneously at all local times. The keograms in the premidnight sector show a prompt response at the onset times, but as we move to earlier and later local time sectors, a substantial delay can be seen between the time of onset and the local auroral response. This behavior is typical for storm-time substorms for which the onsets are "embedded" in a preexisting double-oval configuration [e.g., *Henderson et al.*, 2006].

[50] Although we have clearly demonstrated that the explosive auroral disturbances associated with each tooth are not simultaneously global phenomena, we note that

other types of auroral disturbances can also be seen in the auroral images shown in Figures 4–7. Perhaps the most prominent of these are the intense eastward propagating omega bands which can be seen in the (approximately) midnight to dawn sectors throughout the sawtooth event. These types of auroral forms have long been associated with the substorm recovery phase [*Akasofu*, 1977; *Opgenoorth et al.*, 1994], but as discussed by *Henderson et al.* [2002, 2006], they are also very commonly observed during steady magnetospheric convection (SMC) events. In addition, as shown by *Henderson et al.* [2002], equatorward moving auroral streamers generated at the poleward portions of the double-oval (i.e., "poleward boundary intensifications" or PBIs) can evolve into torch-like structures and omega bands during active times. As pointed out by *Henderson et al.* [2006], omega bands in general tend to be associated with the dynamics of the double-oval configuration whether such a configuration is produced as a remnant of a prior substorm onset (i.e., a recovery phase feature) or is a more long-lived configuration typical of SMC events. We note that all of this type of behavior is observed in the 10–11 August 2000 sawtooth event. As well, due to the cyclical nature of sawtooth events, many of these features can be seen to overlap temporally and spatially. For example, while the first 7 frames in Figure 4 show omega bands in the midnight to dawn sector, the 8th frame shows the development of the localized premidnight equatorward onset in addition to the preexisting omega band forms found farther to the east. Although the omega band forms can be thought of as "recovery phase" features associated with the previous substorm, during sawtooth events they also appear to be prominent preonset features for subsequent teeth. In this regard, omega bands and the underlying magnetospheric conditions associated with them may represent important preconditioners for subsequent onsets and may even act as a catalyst in terms of destabilizing the inner magnetosphere to certain types of instabilities (e.g., ballooning).

2.3. Geosynchronous Dispersion Signatures

[51] In section 2.1, we presented expanded plots of the geosynchronous energetic electron and proton fluxes from the LANL SOPA instruments for each of the teeth. These plots clearly demonstrate that all but the 1845:36 UT (and perhaps the 1330:58 UT) teeth were associated with dispersion signatures consistent with a nightside injection source. In this section, we show that this interpretation holds over the entire energy range measured by the 3 separate LANL instruments (MPA, SOPA, and ESP).

[52] In Figure 11, we present energy versus time spectrograms for each of the LANL spacecraft. Data from all three LANL instruments (MPA, SOPA, ESP) are shown together in the so-called "McIlwain format" in which the electron energies increase up the page while the proton energies increase down the page. Note that for both species, the energies range from a few eV up to several MeV. The rationale for inverting the proton energy axes is that the lowest energy particles of either species follow the same drift trajectories. Thus placing the ≈ "zero" energy particles adjacent to one another allows one to more easily see correlations that may exist between the species at very low energies.

[53] Some caveats concerning the data shown in Figure 11 are important to note. First, the color levels do not represent differential flux. Instead, they represent deviations of the differential flux from an average (energy-dependent) background level. The background levels for each energy channel are computed as a robust average of the log of the flux. The data is presented in this manner in order to enhance energy-time dispersion signatures and the units associated with the color scale are therefore considered to be arbitrary. Second, we have retained the SOPA P1, P2 and P6 energy channels in the energy versus time spectrograms. We have done this for two reasons: (1) at times, the P1 and (particularly) P2 channels show some useful data; (2) the contamination problems associated with these channels show up very clearly in these flux perturbation maps. It is therefore immediately obvious when the P1 and P2 channels should be trusted or not (P6 should never be trusted). For example, strong contamination in the LANL-97A and 1994-084 SOPA P1, P2 and P6 channels is very noticeable as the anomalous horizontal lines in the early part of the day.

[54] From Figure 11a, we can clearly see that numerous energy-time dispersed signatures are evident in both the electron and proton fluxes. These appear as bands of enhanced fluxes that are seen first at high energies and at progressively more delayed times for lower energies. At still lower energies we can also see transitions from the plasmasphere to fresh plasma sheet populations. For example, at 1994-084, the plasmasphere can be identified as the <50 *eV* intense (white) proton band extending from about 0400 to 0830 UT. After 1045 UT, 1994-084 entered the region of the tail where fresh plasma sheet particles have access to. Between 0830 and 1045 UT, weak enhancements in the plasma sheet energy electron fluxes were also observed. This same sequence of features can be seen in the LANL-97A spectrograms as well, except delayed by a few hours because LANL-97A trails 1994-084 by a few hours in orbital phase.

[55] As an interpretive aid, we have schematically highlighted some of the relevant dispersion features in Figure 11b. The onset time associated with each tooth is shown as a dash-dotted vertical line while the dispersion features are drawn as solid or dashed lines. (Dashed lines are used to indicate faint or difficult to follow dispersion traces.) For clarity, we have also used different colors to group features associated with a given tooth.

[56] From Figure 11b we can see that the dispersion patterns are systematically organized. For example, if we focus on the LANL-97A and 1994-084 protons, we can see that the dispersion traces associated with each of the 0041-1030 UT teeth become less and less dispersed as the spacecraft gets closer and closer to the nightside. By the time of the 1030:01 UT onset, the 1994-084 spacecraft was close to the fresh electron plasma sheet access region and saw only a weakly to moderately dispersed pattern. Note that this organization also exists between the spacecraft. For example, for the 0818:06 UT event (yellow lines in Figure 11b), 1989-046 was close to the onset meridian (see Figure 6a) and it saw a dispersionless injection in both protons and electrons. Meanwhile, LANL-97A and 1994-084, which were in the postnoon sector, saw dispersed patterns with more dispersion in the protons at LANL-97A than at 1994-084 and vice versa for the electrons. These

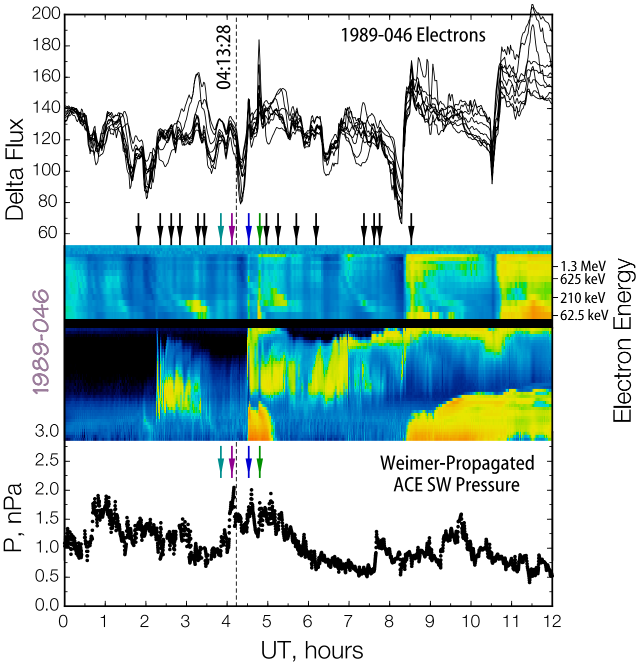

Figure 12. Perturbation electron fluxes at 1989-046 together with Weimer-propagated ACE solar wind dynamic pressure. Note that short-lived (likely pressure induced) dispersionless flux perturbations were occurring nearly continuously for the first 8 hours of the day (arrows). These can be seen most clearly as the vertical stripes in the color energy versus time perturbation spectrogram.

types of dispersion patterns are very similar to those predicted by *Mauk and Meng* [1983] based on the classical injection boundary model and are fully consistent with an injection of particles on the nightside.

[57] Note that the 1845:36 UT event shows no obvious substorm-like electron dispersion, but there is evidence of dispersive features in the SOPA protons. The 1330:58 UT event also does not show clear dispersion, but there does appear to be substorm-like dispersion features following soon after 14 UT.

[58] In addition to substorm-like dispersion patterns, in the LANL geosynchronous data, numerous dispersionless features can occur that are not related to substorms or injections. For example, shocks often produce very easy to recognize global, near-simultaneous dispersionless flux variations at geosynchronous orbit (the 1845 UT event is a rather typical example of this). These have been routinely observed in our data for many years (e.g., see the recent paper by *Huang et al.* [2005]). In addition, sustained continuous dispersionless variations are often seen during disturbed conditions (e.g., storm-time conditions). One of the best ways we have found to display these dispersionless flux variations is in the type of flux perturbation spectrograms shown in Figure 11. From the electrons in the 1989-046 panel, we note that such dispersionless flux variations were occurring continuously for (at least) the first 1/3 of the day (of 11 August). These are easily seen as the vertical stripes in the spectrogram. An expanded version of this is presented in Figure 12.

[59] As can be seen, there are many dispersionless flux variations during this whole time period as indicated by the arrows. (There are in fact more of them and they have more structure than the arrows would indicate). The top shows line plots of the flux perturbations (in arbitrary units) and the bottom panel is a reproduction of the Weimer-propagated ACE solar wind pressure variations (discussed in section 2.6). While no one would expect a perfect match here, we shall see later that it is likely that this pressure profile is a reasonable representation of what actually impinged upon the magnetosphere. Indeed, although the correspondence is far from perfect, we see that some of the pulses in the solar wind match fairly well with some of the dispersionless flux variations seen in the LANL data. What is even more interesting though, is that the major pulses near the 0413:28 UT tooth begin quite substantially before the tooth onset.

[60] An expanded view of this between 0330 and 0600 UT is shown in Figure 13. Here the top set of three curves are the 1989-046 proton flux perturbations (i.e., line plot versions of the data shown in Figure 11) and the next set of seven curves are the 1989-046 electron flux perturbations. The middle three curves are the magnetic field inclination angle at GOES 8 (purple), GOES 11 (blue), and GOES 10 (green) and the bottom curve is the Weimer-propagated ACE solar wind dynamic pressure (see section 2.6). From this plot, we note a number of features. (1) The dipolarization at the three GOES spacecraft are not coherent. There is substantial delay apparent and the structure of the dipolarizations is different at each spacecraft. (2) The two dispersionless spikes visible in the electron fluxes after onset could very well be due to externally imposed solar wind pressure variations. However, it is difficult to temporally match these features with similar features in either the

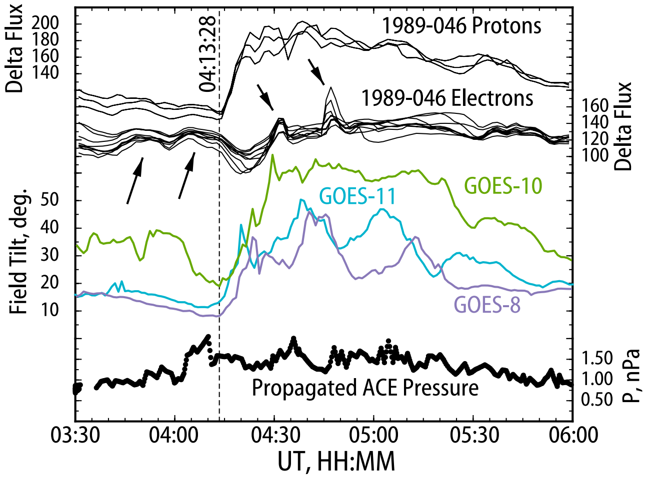

Figure 13. Perturbation electron and proton fluxes measured at 1989-046 together with GOES 10, GEOS 11, and GOES 8 field inclination angles and Weimer-propagated ACE solar wind pressure. The arrows indicate dispersionless features in the electron fluxes that are likely due to local field fluctuations that were likely induced by external pressure variations. Note that the pressure pulses occur substantially before tooth onset and are not well correlated with the GOES dipolarization behavior.

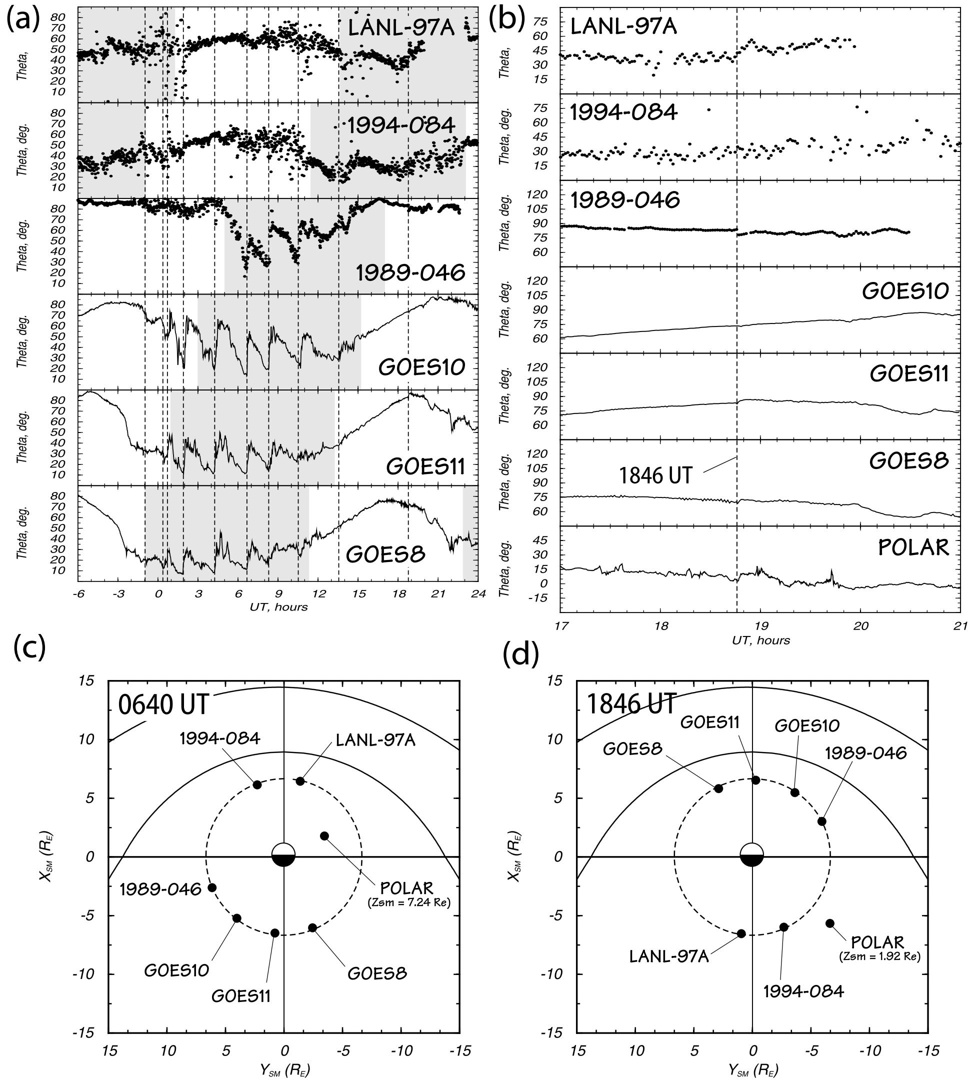

Figure 14. (a) Geosynchronous magnetic field tilt angles at the three LANL and three NOAA GOES spacecraft. The field direction at the LANL satellites is derived from the low-energy magnetospheric plasma analyzer (MPA) particle distribution symmetry axis. (b) A more detailed view of the field tilt angles for the 1845 UT shock event. Field tilt from the Polar spacecraft have also been added. (c and d) Locations of the LANL, GOES, and Polar spacecraft at 0640 UT and 1846 UT.

protons or the GOES inclination angles. (3) The injection-associated dispersion features begin at onset time which is earlier than the two prominent dispersionless spikes. (4) The largest solar wind pressure pulse appears to hit the magnetosphere quite substantially before the tooth onset.

[61] In contrast with these findings, in their analysis of this tooth, *Lee et al.* [2005] matched the largest pressure pulse (near 4UT), with the proton flux increase at 1989-046 and the dipolarizations at the GOES spacecraft. However, we note that they did not propagate the solar wind data at all. Instead they appear to have just assumed that the largest pressure pulse should match the start of the tooth. We do not find this to be the case when a reasonable (and tested) SW/IMF propagation is used. It appears that the subjective mapping assumed by *Lee et al.* [2005] is off by a pulse. In addition, we note that in a related paper, *Lyons et al.* [2005] have a different mapping between the pressure pulses and their putative effects on the magnetospheric behavior. Their mapping is closer to what we present here. On the basis of our more objective solar wind propagation results, we conclude that the largest pressure pulse arrived prior to the tooth onset and therefore likely was not a direct driver for the increases seen at 1989-046 and the three GOES spacecraft at 0413:28 UT. This is also consistent with our finding that the high-latitude duskside auroral feature brightened quite substantially prior to the tooth onset. In our view, a more plausible interpretation is that the pressure pulse (and/or concomitant IMF variations) triggered the substorm and that most of the dispersionless flux variations visible during this and other teeth represent short-lived pressure-induced perturbations to the underlying injection-associated behavior.

2.4. Geosynchronous Dipolarization Signatures

[62] Although the LANL spacecraft do not carry magnetometers, the field direction can be inferred from the

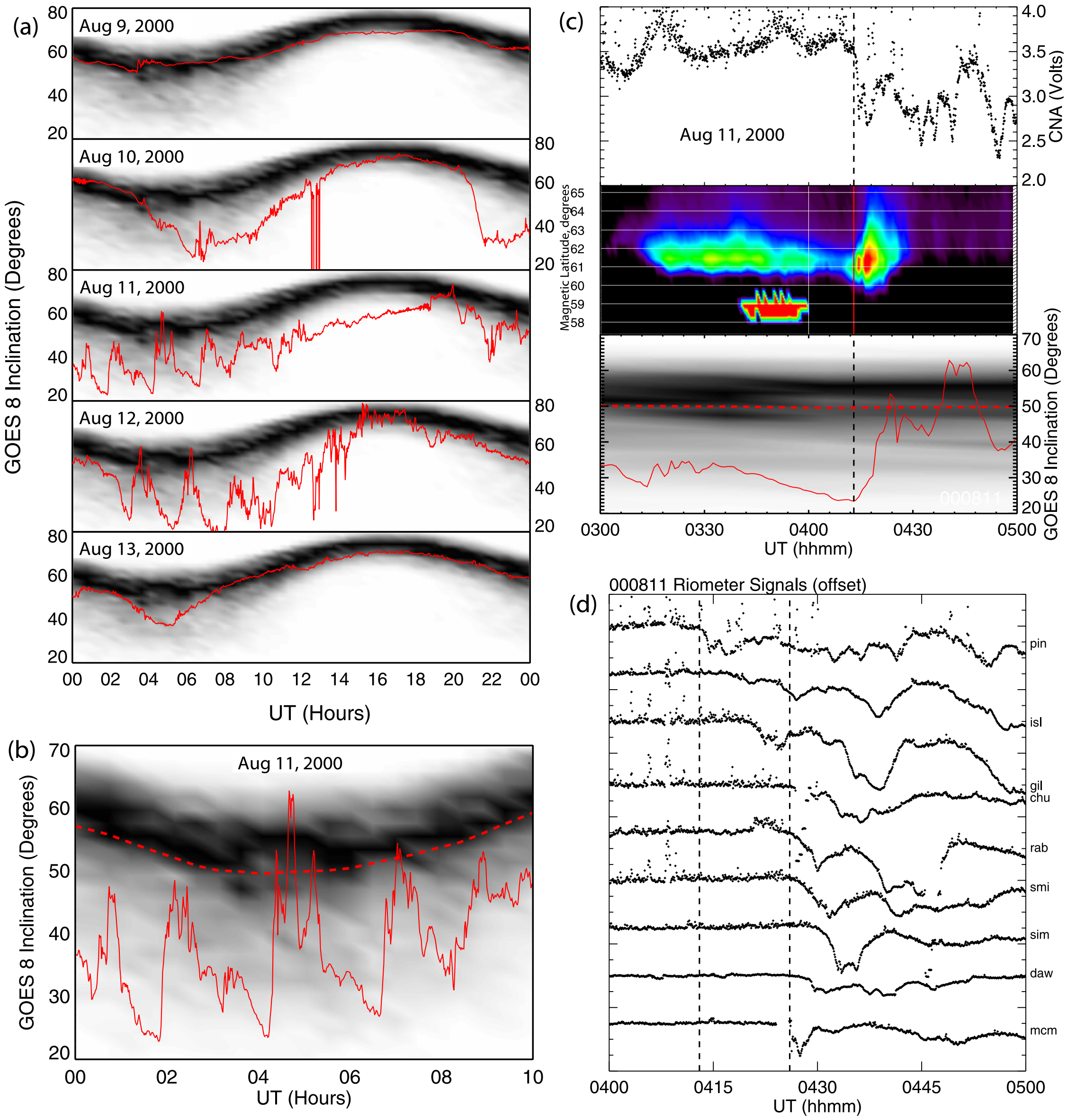

Figure 15. (a) GOES 8 field inclination angle for a 5 day period between 9 August (top panel) and 13 August (bottom panel). The gray scale image is an occurrence frequency histogram over a 280 day interval centered on 11 August 2000. (b) Same as Figure 15a but for 0000–1000 UT on 11 August 2000. (c) Pinawa riometer data (top panel), Pinawa 486 nm meridian scanning photometer data (middle panel), and GOES 8 field inclination angle (bottom panel) between 0300 and 0500 UT on 11 August 2000. (d) Riometer data from selected stations in the NORSTAR array between 0400 and 0500 UT on 11 August 2000.

particle measurements (assuming gyrotropy) when sufficient pitch angle anisotropy exists [*Thomsen et al.*, 1999]. In Figure 14a, we show the field inclination angle at the three LANL spacecraft derived from the MPA particle distribution symmetry axes together with the field inclination angles measured directly at each of the three GOES spacecraft. For the MPA-derived angles, only points are plotted due to the fairly large scatter present and only values for which the $T_{\|}/T_{\perp}$ ratio was less than 0.95 or greater than 1.05 are shown since values of the temperature anisotropy that are closer to 1.0 typically yield unreliable field directions.

[63] In Figure 14a, the time periods during which each spacecraft was situated on the nightside are shaded gray and the onset times associated with each tooth are drawn as vertical dashed lines. An interesting feature that is immediately apparent from this plot is that the tooth-associated strong stretching and dipolarization signatures (i.e., sudden large increases in θ) are typically confined to the nightside. For example, the first significant dipolarization signature seen at 1989-046 was associated with the 0639:06 UT event and that was the first tooth for which the 1989-046 spacecraft was situated on the nightside (see Figure 14c for spacecraft locations at 0640 UT). Meanwhile, the GOES

spacecraft, which moved into the nightside hours earlier than 1989-046 did, observed strong dipolarizations in association with earlier teeth. Note that the LANL-97A and 1994-084 spacecraft appear to show some significant fluctuations in the field inclination angle when they were in the noon-to-dusk sector, but they were relatively small and there is some indication that they were also significantly delayed relative to the nightside signatures observed at the other spacecraft.

[64] The field inclination angle during the 1845:36 UT event is shown in more detail in Figure 14b. In addition to the six spacecraft shown in Figure 14a, we have added the Polar spacecraft which was situated in the postmidnight sector at 1846 UT (see Figure 14d for spacecraft locations). As can be seen, on the dayside the field inclination angle increases slightly at GOES 11 and GOES 8, and but not at GOES 10 and a small decrease was observed at 1989-046. On the nightside, 1994-084 does not show any apparent dipolarization, but LANL-97A and Polar do. Except for at LANL-97A, the dipolarizations are all quite small relative to the earlier teeth. At LANL-97A, the increase in θ is comparable to some of the other teeth, but the field is not initially as stretched. In addition, unlike the other teeth, the increase appears to be a relatively transient phenomenon on the leading edge of a more gradual relaxation of the stretched field at LANL-97A. This behavior can be seen more clearly in Figure 14a.

[65] Figure 15a shows the field inclination angle at GOES 8 for a 5 day period from 9 to 13 August 2000. Each panel represents one day (with 9 August at the top and 13 August at the bottom). The field inclination angle is shown as a solid red line and the background image in each panel is an occurrence frequency histogram of the GOES 8 field inclination angle observed over a 280 day period centered on 11 August 2000. The region of highest occurrence frequency appears as a sinusoidal black band with a minimum on the nightside and a maximum on the dayside, i.e., the field is more stretched on the nightside and more dipolar on the dayside as is well known. On the nightside there is also an enhanced occurrence frequency extending to much lower angles and this is due to stretching events like substorms. Comparing the red traces with the histogram in each panel, it is clear that the tail stretching associated with this sawtooth event was amongst the most extreme during the 280 day span surrounding it. In addition, we note that on the 11th when GOES 8 is on the dayside (≈1200–1800 UT) the histogram shows that the field becomes much more stretched than is typical. This indicates that sawtooth events can produce very rare dayside stretching as well, although the field lines do not become tail-like as they do on the nightside.

[66] A more detailed view of the GOES 8 nightside dipolarizations on the 11th is shown in Figure 15b. In this plot, the dashed red line is the mean inclination angle associated with the 280 day histogram. Note that for some of the dipolarization events, the field does not return to this nominal value indicating that for some of the teeth, the tail can remain somewhat more stretched than usual even after the dipolarization.

[67] Figure 15c shows the GOES 8 field inclination angle between 0300 and 0500 UT on 11 August together with the 486 nm Meridian Scanning Photometer (MSP) data from Pinawa. Although the quality of the MSP data is substantially reduced because the moon is up and there is some atmospheric haze, there is no doubt that the proton aurora (as monitored at 486 nm) is over Pinawa. This is noteworthy because the proton aurora is only very rarely seen at such low latitudes. At 0413 UT, a brightening occurs which is associated with a poleward retreat of the proton aurora. The poleward motion of the proton auroral boundary indicates a dipolarization of the tail field which is consistent with the GOES 8 measurements shown in the bottom panel of 15c.

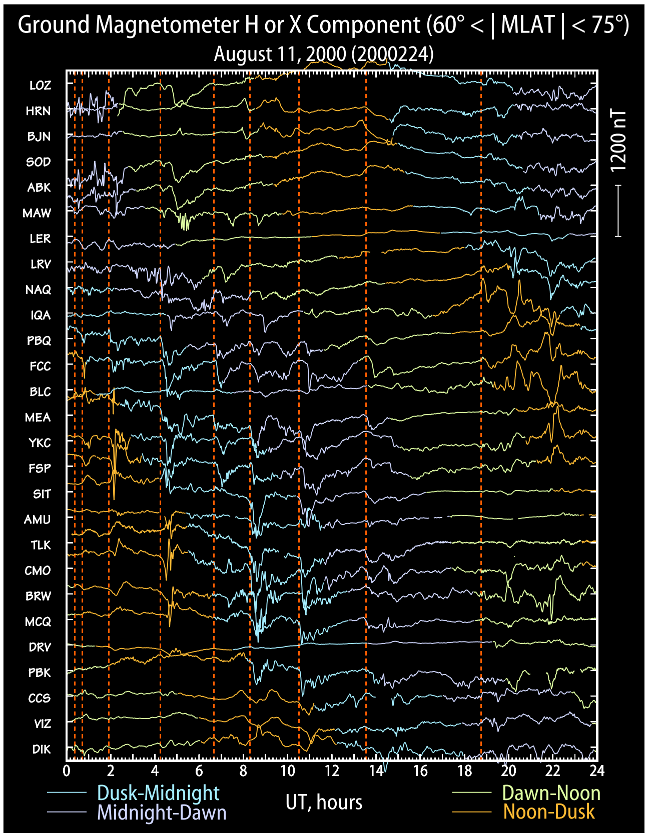

Figure 16. Ground magnetometer data from 27 auroral zone stations between magnetic latitudes of 60°–75° and −60° to −75°. The X or H component from each station is shown. The ticks on the vertical axis are 600 nT apart, and a nominal baseline (computed as a robust average over the entire day) has been subtracted from each station. Line colors indicate the (time-dependent) MLT sector of each station: Blue, purple, green, and orange correspond (respectively) to 18–24 MLT, 00–06 MLT, 06–12 MLT, and 12–18 MLT.

[68] Riometer data from Pinawa and other locations in the Canadian NORSTAR array are also shown in Figures 15c and 15d. It is interesting to note that although a prompt absorption signal was observed at 0413 UT at Pinawa, the other stations did not observe a drop until at least 5 min later. The absorption signal can then be seen expanding poleward and westward in typical substorm fashion. This clearly demonstrates that the absorption onset effects were initially localized in latitude to Pinawa for at least 5 min. Furthermore, the Fort McMurray (MCM) station is only about 4° (of CGM latitude) poleward and 23° west of

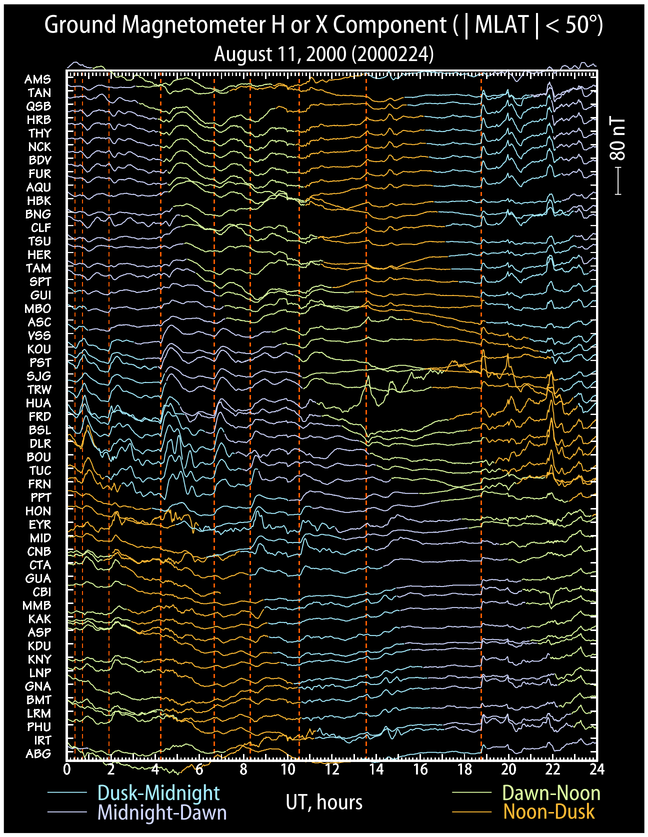

Figure 17. Ground magnetometer data from 51 low- to middle-latitude stations (magnetic latitudes between −50° and 50°). The X or H component from each station is shown. The ticks on the vertical axis are 40 nT apart, and a nominal baseline (computed as a robust average over the entire day) has been subtracted from each station. Line colors indicate the (time-dependent) MLT sector of each station: Blue, purple, green, and orange correspond (respectively) to 18–24 MLT, 00–06 MLT, 06–12 MLT, and 12–18 MLT.

Pinawa. and it does not see an absorption until a lot later (bottom trace in Figure 15d).

2.5. Ground Magnetometer Data

[69] Figure 16 shows 1 min resolution H or X component ground magnetometer data from 27 auroral zone stations between magnetic latitudes of 60°–75° and −60° to −75°. The entire day of 11 August is shown and the traces have been color-coded to indicate the MLT sector of the observing station as a function of time. The blue and purple colors indicate that a station was in the dusk-midnight and midnight-dawn sectors respectively (i.e., on the nightside), while the green and orange colors indicate that it was in the dawn-noon and noon-dusk sectors respectively (i.e., on the dayside). From Figure 16 it is clear that many of the teeth were associated with obvious intense negative "H bays" and that these H bays were typically most intense when they were observed on the nightside. In addition, they were also not globally simultaneous, but rather they tended to develop in the premidnight sector first. We note also that there was no obvious substorm-like signatures associated with the 1845:36 UT event.

[70] A similar plot of the 1 min resolution low- and middle-latitude H or X component ground magnetometer data from 51 stations between magnetic latitudes of −50° to 50° is presented in Figure 17. Here, we also see that the most intense positive "H bays" tend to occur on the nightside or are skewed toward the dusk-midnight sector. At other locations, smaller negative or "transitional H bays" (i.e., bays with both positive and negative excursions [*Rostoker*, 1966]) are observed. In addition, it is extremely clear from this plot that most of the teeth were not associated with a globally simultaneous onset of positive H bays. For example, during the 0413:28 UT event, the strongest and most prompt increases in H were observed in the premidnight sector over the eastern half of the North and South American continents (e.g., at San Jaun (SJG), Fredricksburg (FRD) and Korou (KOU)). However, as one moves away from this region the H bays decrease in strength and are observed at progressively more delayed times. This type of behavior is completely consistent with substorm activity and we note that the strongest positive H bays for the 0413:28 UT event occurred in exactly the same sector as the auroral onset shown earlier in Figure 4.

[71] In sharp contrast to the earlier events (including the 0413:28 UT event), for the 1845:36 UT event, Figure 17 clearly shows that a positive-going impulse was observed nearly simultaneously at all local times. This type of activity is not consistent with a substorm, but is consistent with the arrival of a sudden solar wind pressure enhancement and as shown previously in Figure 9 the geosynchronous and auroral behavior is also fully consistent with this interpretation. For the 1330:58 UT event, the ground magnetometer data shows some auroral zone negative H bay activity on the nightside (see Figure 16) but the low- and middle-latitude stations show only very weak positive H bays in the midnight to postdawn sectors (see Figure 17) and it is again unclear exactly what happened during this event.

[72] Although we have already presented the auroral electrojet index in Figure 1, it is important to recognize that this index is derived from only 12 auroral zone stations. As is well known, this limited spatial coverage means that the spatial and temporal behavior of the auroral electrojets is not always well characterized by AU and AL. Furthermore, while the standard AU and AL indices are always defined by a single contributing station at any given time (with different stations contributing to AU and AL), the magnetic local time of the contributing station is not specified. In order to increase the spatial coverage and in order to determine the MLT of the contributing stations for the 11 August sawtooth event, we have constructed a 27-station version of the standard AU and AL envelope indices (hereafter referred to as AU^* and AL^* to avoid confusion with the real AU and AL indices). The results are shown in Figure 18. AU^* and AL^* are shown in the first two panels, while in the bottom panel we have plotted the magnetic local time of the station that contributed to each index. As with the standard AL index, the AL^* index in Figure 18 shows prompt substorm-like negative excursions in association with the 0151 UT to 1330 UT events. Less intense positive excursions in AU^* are also observed. The behavior of AU^* and AL^* for the 0041 UT event is more complex and

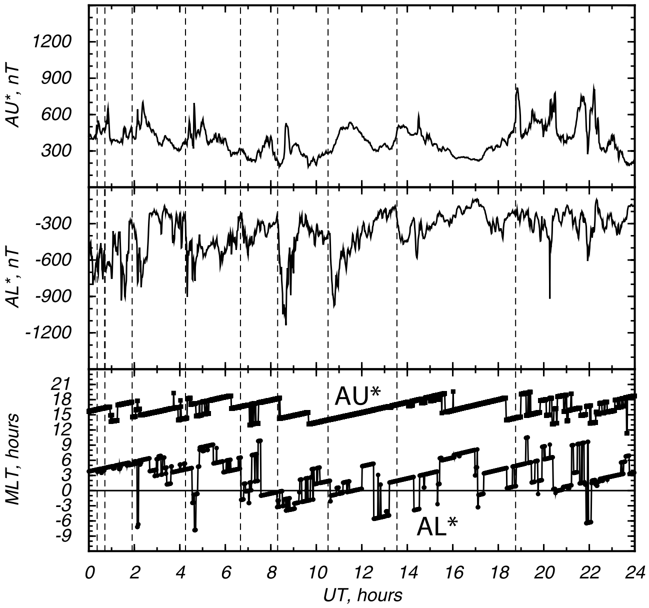

Figure 18. AU- and AL-like envelope of traces for the 27 auroral zone stations shown in Figure 16. The curve in the middle (top) panel shows the minimum (maximum) value that was attained at any of the 27 stations as a function of time. To avoid confusion with the standard AU and AL indices, we have labeled the curves *AL** and *AU**. The bottom panel shows the magnetic local time of the stations contributing to *AL** and *AU**.

difficult to interpret and for the 1845 UT event, the response in *AU** is dominant and pulse-like while the response in *AL** is not very substorm-like.

[73] From the bottom panel in Figure 18 we can see that the magnetic local time of the *AU** contributing station is relatively well behaved and confined (approximately) to the 12–21 MLT sector. This is consistent with AU being produced mainly by the DP2-associated eastward electrojet. In contrast, there is much more variability present in the MLT of the *AL** contributing station. Specifically, a jump to earlier, premidnight locations is observed following each of the onsets between 0151 UT and 1030 UT. Since during disturbed conditions, the AL index is most often contributed to from stations located near 0300 MLT [*Allen and Kroehl*, 1975; *Akasofu et al.*, 1980], this type of behavior is indicative of the establishment of a new substorm-associated westward electrojet in the premidnight sector in association with each of these onsets (e.g., see *Kamide* [1988, chap. 3, and references therein] or the more recent study of *Gjerloev et al.* [2004]). Thus the 0151 UT to 1030 UT events appear to have been associated with the development of a substorm (or DP1) current system on top of the preexisting DP2 current system. Note that the 0041, 1330 and 1845 UT events do not show evidence of such a jump.

[74] Another index that has been used in recent years to infer variations in the DP2 current system is the Polar Cap or PC index [*Troshichev et al.*, 1979, 1988]. This index is derived from the horizontal variations observed at a single polar cap magnetometer station. In the Northern Hemisphere, the Thule magnetometer station is used to derive the PCN index (N for northern) while in the Southern Hemisphere, the Antarctic Vostok station is used to derive the PCS index (S for southern). In Figure 19 we present the Thule horizontal components together with the PCN index. As can be seen, a significant increase in the PCN index occurs at or following each of the 0151–1845 UT events. Although such increases have been used to indirectly infer the occurrence of solar wind pressure pulse hits on the magnetosphere [e.g., *Lee et al.*, 2004] or IMF changes that affect the polar cap ionospheric electric field [*Troshichev et al.*, 2000], we have already shown that, for the 0151 to

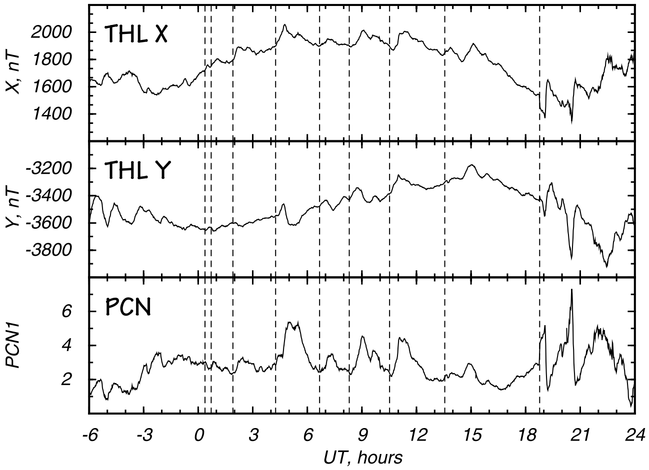

Figure 19. X and Y component magnetogram traces from Thule together with the 1 min PCN index (which is derived from the Thule horizontal components.

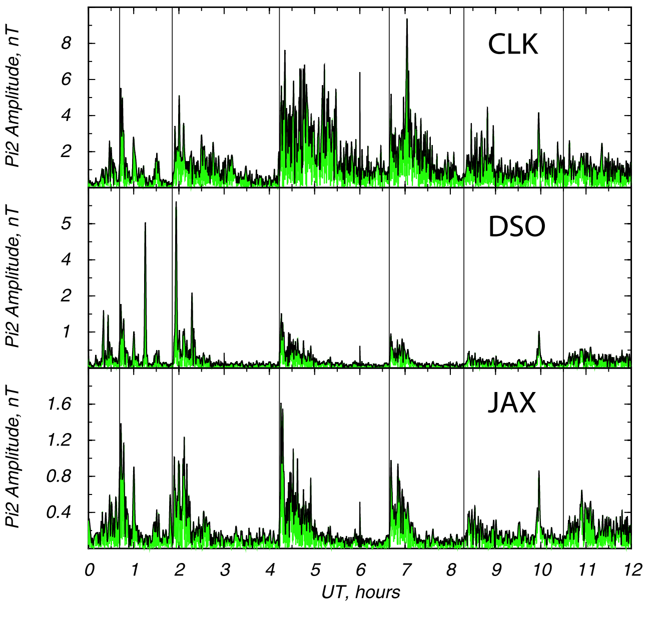

Figure 20. One second Pi2-filtered ground magnetometer data from the CLK, DSO, and JAX stations in the MEASURE array. The horizontal components have been summed, and the green line is the Pi2 band-pass-filtered horizontal component power (which oscillates at twice the Pi2 frequency). The black line is a spline fit to the envelope of power.

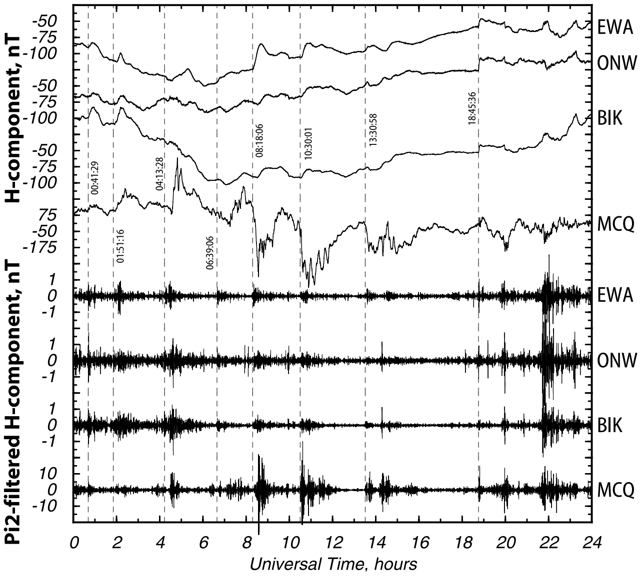

Figure 21. One second resolution ground magnetometer data from Ewa Beach (EWA), Bikia (BIK), Onagawa (ONW), and MacQaurie Island (MCQ). The top four traces show the unfiltered H components, while the bottom four traces show the Pi2-filtered (40–150 s) H components. Note the scale change for MCQ.

1030 UT events, a DP1 (or substorm-associated) current system developed on the nightside. The fact that the increases in PCN associated with those events all occur at or following the onsets indicates that they are likely to have been produced by a substorm-associated current system (or a combination of DP1 and DP2 increases) rather than a large-scale response of only the DP2 system. Although this interpretation is at odds with some studies that claim the PC indices do not respond appreciably to substorms [e.g., *Liou et al.*, 2003], it is consistent with the recent work of *Huang* [2005] and other studies that have shown a high correlation between increases in the PC index and substorm occurrence [e.g., *Troshichev et al.*, 1979; *Troshichev and Lukianova*, 2002]. We note also that the 1845 and 1330 UT events show an increase in PCN and these may well have been due to pressure hits or IMF changes as we shall see in the next section.

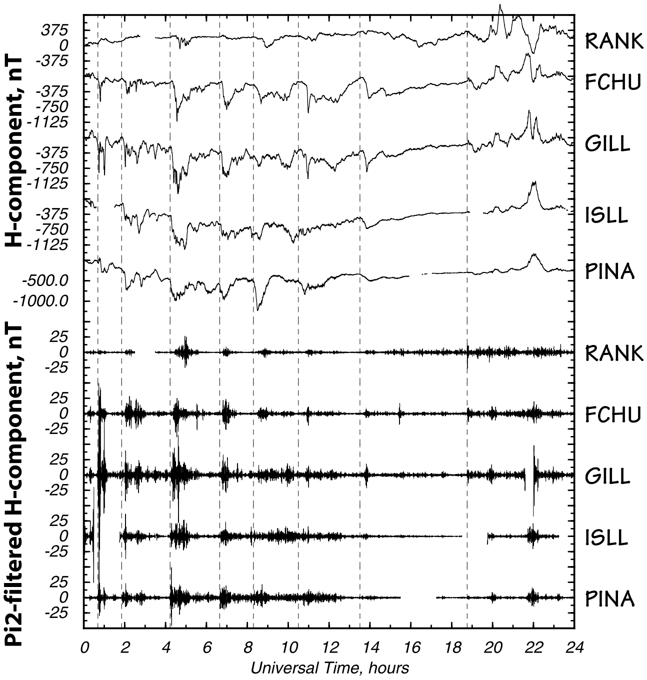

Figure 22. Five second resolution ground magnetometer data from the CARISMA Churchill line. The top five traces show the unfiltered X components, while the bottom five traces show the Pi2-filtered (40–150 s) X components.

[75] Next, we present high-resolution magnetometer data from the U.S. East Coast Measure Array. Figure 20 shows 1 s Pi2-filtered ground magnetometer data from the CLK, DSO, and JAX stations. For each station, the two horizontal components have been added and their power is plotted as a green line in each panel. The upper envelope of the green trace is shown as the black line and was derived as a spline fit to the envelope of the power curves. During the time period surrounding the 0041 UT tooth, we can see that there were multiple Pi2 bursts. Although the strongest of these corresponds to the 0041:29 UT event, it is clear that the activity was fairly complex and difficult to interpret. For the other teeth shown in Figure 20, the onset of Pi2 ULF pulsations is much clearer.

[76] In Figure 21, we present selected high-resolution magnetometer data from the Japanese 210MM magnetom-

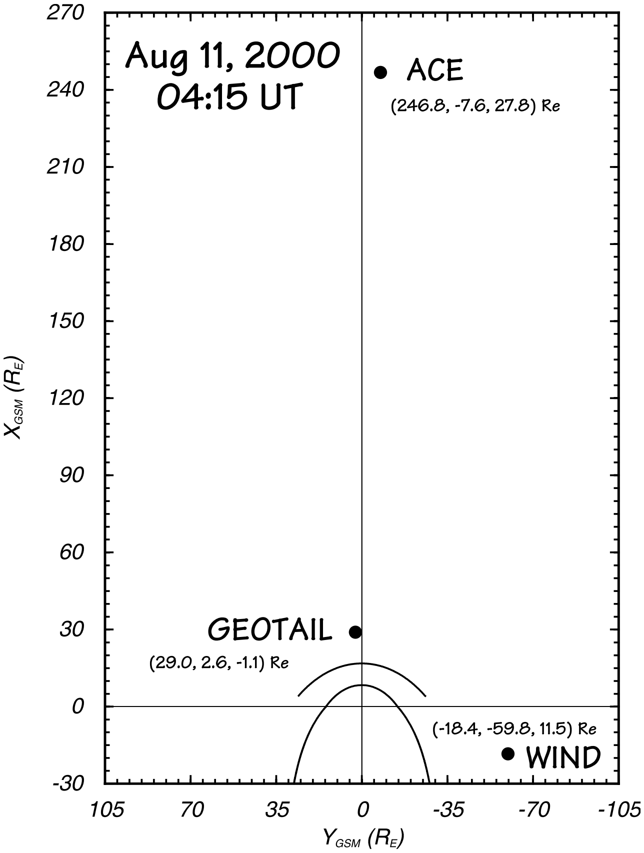

Figure 23. Locations of ACE, Geotail, and Wind at 0415 UT, 11 August 2000.

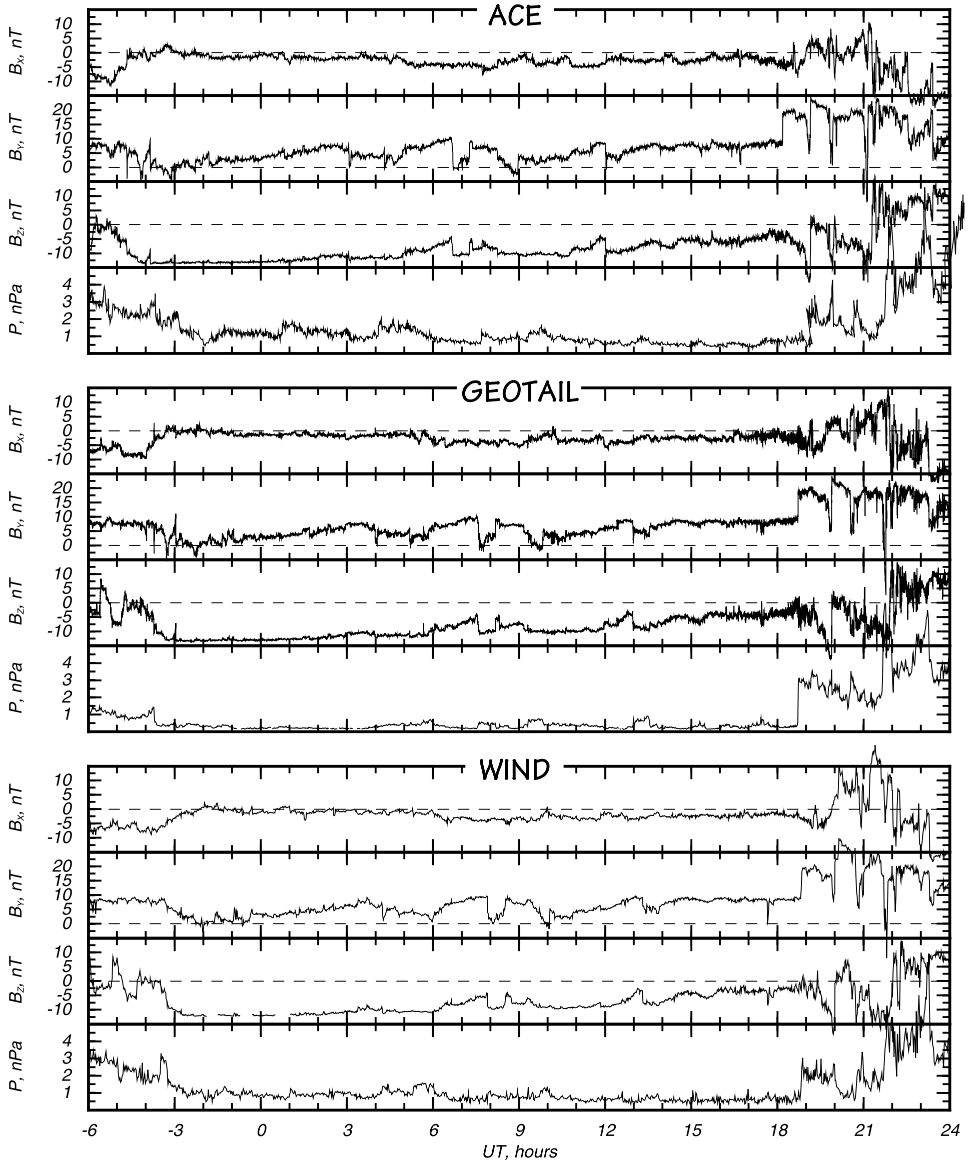

Figure 24. IMF and solar wind dynamic pressure data from the ACE, Geotail, and Wind spacecraft. The time shown ranges from 1800 UT on 10 August to 2400 UT on 11 August 2000.

eter network and the Canadian CARISMA (formerly CANOPUS) network. One second resolution H component data from Ewa Beach (Hawaii), Onagawa, Bikia and MacQuarie Island are shown in Figure 21 in their raw form (top four traces) and in their Pi2 bandpass (40–150 s) filtered form (lower four traces). In Figure 22, 5 s X component data from five stations in the 'Churchill line' (Pinawa, Island Lake, Gillam, Fort Churchill, and Rankin Inlet) are shown in a similar format. In both Figures 21 and 22, we can see that the onset of each event was associated with the occurrence of a Pi2 pulsation and either negative or positive H bays. Note also that the Pi2 pulsations do not occur at the same time everywhere. For example, Pi2 pulsations associated with the 0413:28 UT event begin promptly at Pinawa in conjunction with the sharp onset of a negative H bay. However, as one moves poleward along the Churchill line, both the onset of the H bay and Pi2 pulsations becomes more delayed. This behavior is very similar to that reported by *Olson and Rostoker* [1977]. The positive H component bays seen in the 210MM network for this event are also substantially delayed.

2.6. IMF and Solar Wind Conditions

[77] During this event, ACE, Geotail and Wind were all situated in the solar wind. As shown in Figure 23, at 0415 UT on 11 August, ACE was far upstream at R_{GSM} = (246.8, −7.6, 27.8) R_E while Wind and Geotail were situated closer to the Earth at R_{GSM} = (−18.4, −59.8, 11.5) R_E and R_{GSM} = (29.0, 2.6, −1.1) R_E respectively. The interplanetary magnetic field (IMF) (in GSM coordinates) and solar wind (SW) dynamic pressure variations from these spacecraft are shown in Figure 24. In this overview plot, none of the data have been time shifted to account for propagation delay times. Nevertheless, we can see that the behavior of the IMF at each location is very similar. At ACE, the IMF turns southward before 1900 UT

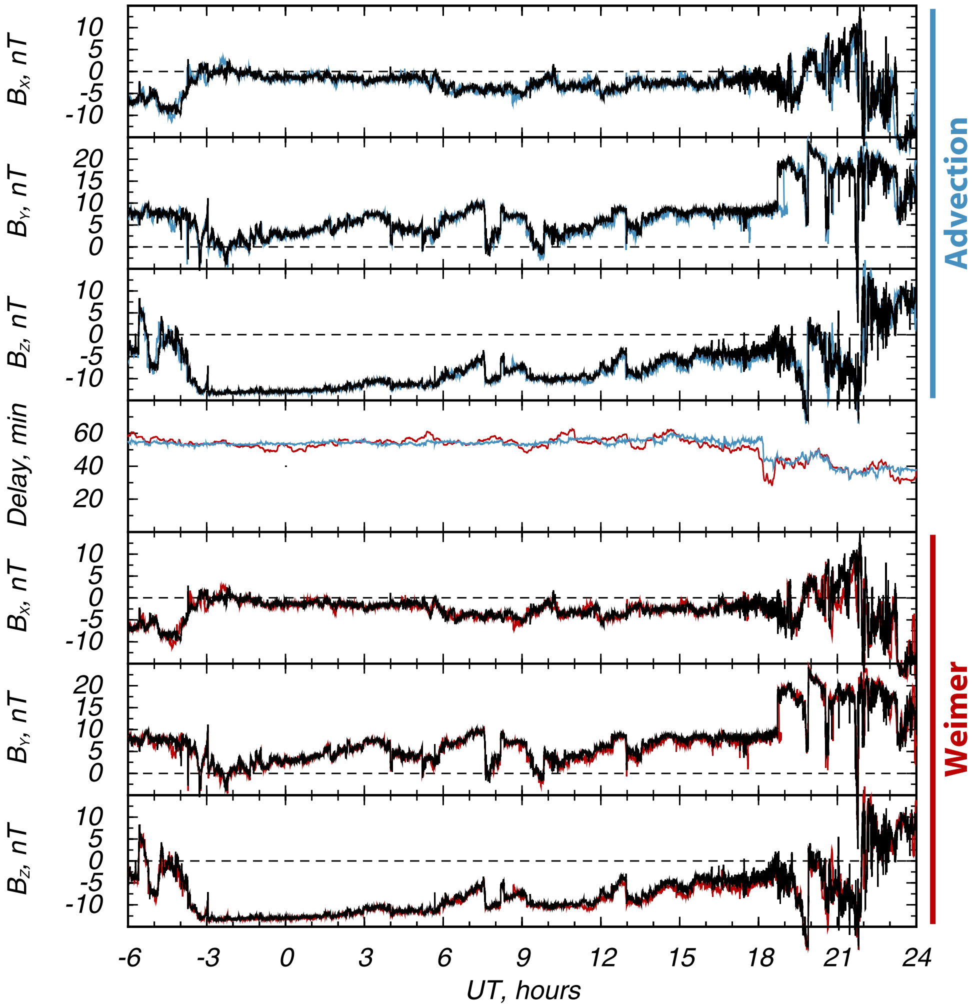

Figure 25. IMF at ACE propagated to the location of Geotail. The blue lines result from propagating the ACE data with simple advection. The red lines are obtained from a modified Weimer method. The Geotail data are shown in black. The delay times derived for the advection and Weimer propagation methods are shown in the fourth panel.

on 10 August 2000 and remains negative for approximately 24 hours afterward. Up until about 0500 UT on 11 August, the IMF is moderately to strongly southward (≈ -13 nT) and quite steady. After 0500 UT, the strength of the B_z component decreases and a number of fluctuations and discontinuities are observed, particularly in the B_y and B_z components. Just after 1800 UT, a shock was observed at ACE which produced a very abrupt increase in the field strength (mostly in B_y) and a simultaneous increase in the dynamic pressure. Except for a time delay, this behavior is essentially the same at all three spacecraft.

[78] In addition to the large shock-associated increase just after 1800 UT, the SW dynamic pressure at ACE exhibits a number of more gradual increases and decreases between 1900 UT on 10 August and 0600 UT on 11 August. These pressure fluctuations are not evident in either the Geotail or Wind pressure data, but we note that Wind was substantially far off from the Earth-Sun line, and the Geotail pressures during this time period seem anomalously low compared to either ACE or Wind and may not be as robust as the ACE measurements In any case it is interesting to note that although the pressure fluctuations seem to be poorly correlated between the three spacecraft, the IMF measurements appear to be very well correlated.

[79] In order to obtain a more accurate representation of the IMF and SW variations that actually impacted the Earth, we applied the *Weimer et al.* [2002] variable time delay propagation method to the ACE-Geotail and ACE-Wind satellite pairs. In Figure 25 we show the results of this analysis for the ACE-GEOTAIL pair in a format similar to that used by *Weimer et al.* [2002]. The Geotail data is shown in black in the top and bottom three panels. The blue lines are the ACE IMF data propagated with the simple advection-derived delay time (blue line in center panel). The red lines are the ACE IMF data propagated with the variable time delay (red line in center panel) obtained via a modified *Weimer et al.* [2002] method. The variable time delay was obtained by optimizing the match between only the B_y and B_z components and by reducing the initial segmentation to 1 hour intervals rather than the 6-hour intervals used by *Weimer et al.* [2002]. In addition, we restricted the time adjustments for each iteration to be ±5% for all times except

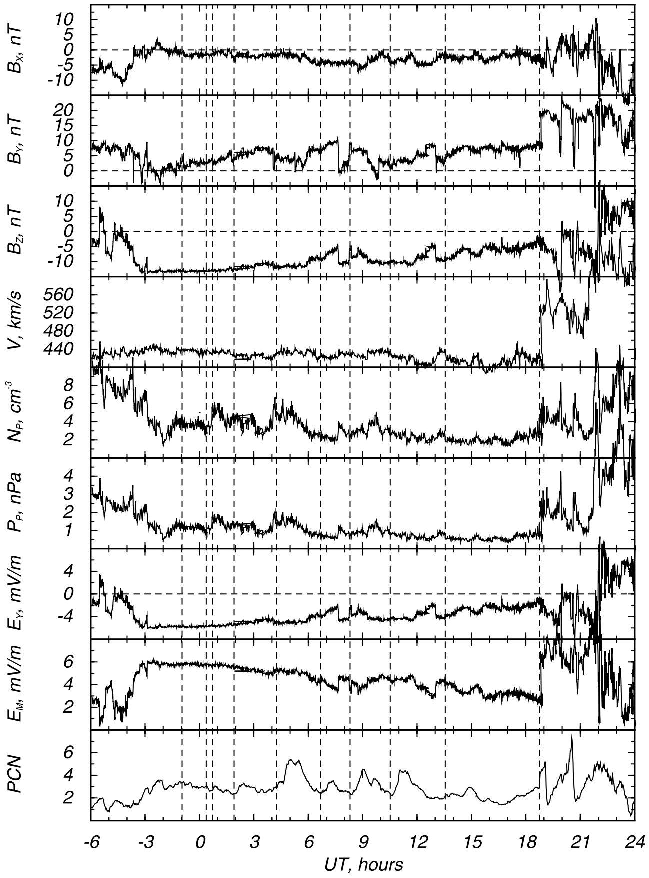

Figure 26. IMF and SW measurements at ACE propagated to $X_{\mathrm{GSM}} = 10\ R_E$.

between 1800 and 1930 UT on 11 August. In order to capture the shock in this interval we increased the allowable time adjustments to be ±30% there. These modifications were made because the rapid fluctuations at and following the shock seemed to confuse the unmodified algorithm and actually made the matches worse.

[80] The variable time delay obtained from the ACE-Geotail analysis was used in conjunction with the observed solar wind speed to propagate the ACE IMF and SW data to the vicinity of the Earth's dayside magnetopause (we adopted a constant value of $X_{GSM} = 10\ R_E$). The results are shown in Figure 26. The first seven panels show the IMF components (in GSM coordinates), the solar wind speed, the proton number density, the proton-derived dynamic pressure and the y component of the SW electric field. The eighth panel shows the so-called "merging electric field" which is defined as

$$E_M = V\left(B_y^2 + B_z^2\right)^{1/2} \sin^2(\theta/2) \qquad (2)$$

where $\theta = \tan^{-1}(B_y/B_z)$ [e.g., *Kan and Lee*, 1979]. For comparison, the ninth panel in Figure 26 shows the PCN index which is supposed to be sensitive to variations in the merging electric field and/or SW dynamic pressure fluctuations [*Troshichev et al.*, 2000; *Huang*, 2005]. The vertical dashed lines are the tooth onset times as before.

[81] One can immediately see that the 1846 UT event matches precisely with the shock observed by ACE. In addition, the 0041 UT and 0413 UT teeth appear to be associated with increases in the dynamic pressure and the 0810 UT event appears to have been associated with a sudden reduction in the merging electric field (i.e., northward turning of the IMF). For the other events, there is no obvious correlation with the IMF and SW variations. On the other hand, (as we have already mentioned) there is a strong correlation between the teeth and variations in the PCN index. This suggests that the PCN index may not always respond only to variations in the IMF and SW as has been assumed by others [e.g., *Lee et al.*, 2004]. For example, from Figure 26, we can see that there was an abrupt increase in both the merging electric field and the dynamic pressure at around 0730 UT, but there was no apparent response visible in the PCN index at that time. On the other hand, the 0639 UT tooth was not associated with an obvious IMF or SW disturbance and yet it was associated with a significant increase in the PCN index. This seems to suggest that the PCN index can also respond to a significant degree to the substorm associated DP-1 system as well as the convection associated DP-2 system.

[82] In the recent study of *Lyons et al.* [2005], they suggested that potential triggers in the solar wind and IMF could be cancelled out in a variety of ways. For example, if a northward turning is accompanied by a pressure reduction, then the trigger is nullified. Although this is an interesting hypothesis, we note that the "null" events they identified during this event all occurred at times when the field was still stretching. Thus another interpretation for why no substorms occurred in association with those disturbances is that the magnetosphere was stable and not yet receptive to external triggering. In addition, we note that the "NULL4" event identified by *Lyons et al.* [2005] appears to be just an artifact of the GSE coordinate system used by them to plot the Geotail data. Here we have plotted the IMF data in GSM coordinates and we do not see a northward turning just prior to 10UT as they claim. Although this does not invalidate their hypothesis on nullifying effects, it does diminish the observational support for it.

3. Discussion and Conclusions

[83] In this paper, we have examined each of the flux enhancements associated with the 10–11 August 2000 sawtooth event in detail. We find that all but one of the teeth were associated with injections at geosynchronous orbit, and that most of the teeth were consistent with the hypothesis that they are predominantly caused by unusually large and longitudinally extended substorms. A few were unclear or complex, and the final flux enhancement at 1845:36 UT was not a substorm but a solar wind shock-associated disturbance. In addition, the presence of numerous dispersionless flux perturbations in the LANL SOPA data provides support for the hypothesis that solar wind pressure variations can modulate the flux profiles to some extent.

[84] For the substorm events we find that the geosynchronous particle flux behavior is not simultaneously dispersionless around the globe. We also showed that the strong onset-associated geosynchronous magnetic field

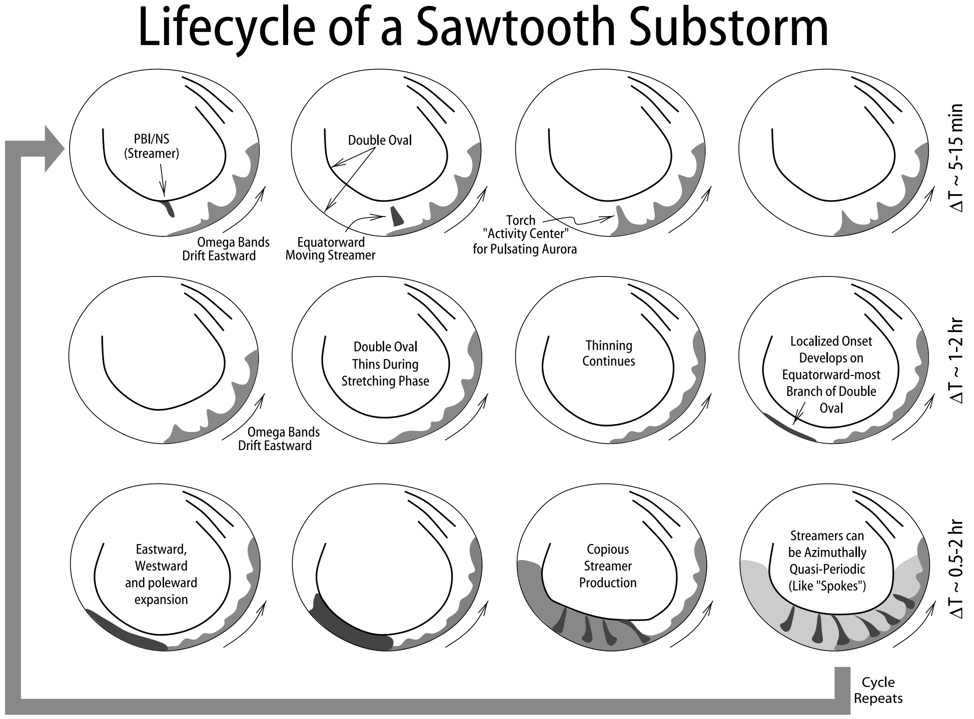

Figure 27. Highly simplified schematic representation of the life cycle of a sawtooth substorm.

dipolarization signatures are typically confined to the nightside and are particularly strong when the observing spacecraft was situated in the premidnight sector. Although dipolarization signatures were seen on the dayside for some events, they were generally weaker and delayed in time relative to the onset of the nightside dipolarizations. When global auroral imager data was available, all of the substorm events displayed unambiguous storm time ‘‘embedded substorm onsets’’ in the dusk-to-midnight sector and subsequently expanded eastward, westward and poleward in typical substorm fashion. In addition, auroral zone and middle to low-latitude ground magnetometer data showed typical storm-time substorm behavior including high-latitude negative H bays, middle- and low-latitude positive H bays, and a partial recovery in Sym-H associated with each tooth. In addition, each substorm tooth was associated with the onset of Pi2 ULF pulsations.

[85] For the final shock-associated flux increase, we found that the geosynchronous particle fluxes increased in a globally, near-simultaneous manner. However, the flux increases, particularly for electrons, were weak in comparison to the substorm-associated events. Also, as expected, there was a significant and prompt increase in the magnitude of the magnetic field throughout the inner magnetosphere and only a very weak and transient dipolarization signature was observed. Global auroral imager data available during this event also showed a global brightening of the aurora together with the onset of some high-latitude auroral dynamics, as expected. However, no substorm was observed to develop in association with this activity. It is important to note that such shock-associated disturbances are not uncommon, especially during storm periods. On the other hand, solar wind shocks are not typically seen to occur with a characteristic 2–4 hour periodicity. Although it was apparent from the outset that the last flux increase was shock induced (and did not look very much like a typical ‘‘tooth’’), we included it in our analysis in order to exemplify the differences between such events and typical periodic sawtooth disturbances.

[86] In order to more clearly illustrate the typical auroral behavior associated with sawtooth substorms, in Figure 27 we present a highly simplified schematic representation of the auroral distribution during the course of a single tooth. Since this cartoon is meant to depict the types of processes that can occur, the time between each frame is not uniform. The top four frames span a time interval of 5–15 min or so and are meant to illustrate how auroral torches and omega band structures are related to PBIs (Poleward Boundary Intensifications) and equatorward moving auroral streamers. As shown by *Henderson et al.* [2002], auroral streamers ejected equatorward from the poleward portion of a double-oval configuration can evolve into auroral torches and omega band structures. Active and dynamic double-oval distributions are commonly observed during SMCs (Steady Magnetospheric Convection events) and can develop as a result of prior substorm activity.

[87] The middle four frames in Figure 27 span a time period of 1–2 hours and show how the double-oval configuration thins in latitudinal extent during the stretching phase leading up to the tooth onset. Onsets like this have been referred to as ‘‘embedded onsets’’ or ‘‘deeply embedded onsets’’ [e.g., *Murphree et al.*, 1993; *Henderson et al.*, 2006] because they occur well away from the open field line region and are ‘‘embedded’’ in the most equatorward portions of a preexisting double-oval auroral configuration. Note that such a morphology is fully consistent with the Akasofu description of onset occurring on the most equatorward arc. Note also, that the onset region, in the premid-

Table 2. The 10–11 August 2000 Sawtooth Timing

Event	Time, UT	Timing Method	Dispersed Injection	Auroral Onset	Event Type	Potential Trigger
1	2302:25[a]	YOR 1s H component Pi2	yes; nightside source	unknown	substorm	none obvious; B_y increase?
2	0041:29	GOES field tilt	yes; nightside source	unknown	substorm	pressure increase
3	0151:16	GOES field tilt	yes; nightside source	yes	substorm	none obvious; B_y?
4	04:13:28	GOES field tilt	yes; nightside source	yes	substorm	pressure increase, B_y?
5	0639:06	BIK 1s H component Pi2	yes; nightside source	yes	substorm	none obvious; E_M?
6	0818:06	GOES field tilt +1989-046	yes; nightside source	yes	substorm	B_z northward turning, B_y increase
7	1030:01	MCQ 1s H component Pi2	yes; nightside source	yes	substorm	none obvious; B_y?
8a	1330:58	MCQ 1s H component Pi2	not sure	unknown	not sure	pressure decrease?
8b	1410:20	MCQ 1s H component Pi2	yes; source not clear	unknown	not sure	none obvious
9	1845:36	YOR 1s H component	no; globally dispersionless	no	IMF/SW Shock	SW shock

[a] Date is 10 August 2000. All other times are on 11 August 2000.

night sector, is localized but develops adjacent to the broadly distributed omega band region farther to the east. The often observed coexistence of these features may lead to a perception that the onset region is far wider than it really is.

[88] The bottom four frames in Figure 27 span a time period of between 0.5–2 hours and show how the expansion phase typically evolves during sawtooth events. Although the auroral bulge expands eastward, westward and poleward in fairly typical substorm fashion, a conspicuous feature present during sawtooth substorms is the copious production of auroral streamers. While these also commonly occur during isolated substorms, they are much more intense and abundant during the late expansion phase of sawtooth substorms. They can occur in fairly complex groupings, but are also frequently seen to occur in prominent quasiperiodic azimuthal “spoke-like” patterns. As discussed by *Henderson et al.* [2002], these features are likely the result of earthward propagation of BBFs in the tail which in turn are likely due to depleted (low-PV^{γ}) flux tubes generated as a result of localized and/or patchy reconnection at an X line. We surmise that the copious production of these features during sawtooth substorms is due to sustained, driven tail reconnection and that their sometimes prominent spatial periodicity may reflect a spatially periodic modulation of the reconnection rate, perhaps due to wave-modulated boundary conditions near the reconnection region.

[89] It is interesting to note that much of the auroral phenomenology portrayed in Figure 27 also applies quite well to active intervals of SMC or “convection bay” events. During SMCs, however, there can be no localized substorm-like onsets by definition. Instead, the auroral dynamics during SMCs behaves much like the activity seen during the late expansion phase or early growth phase of sawtooth substorms, including the generation of streamers, torches and omega bands. Also note that if the time between successive teeth during sawtooth events were to increase above about 4–6 hours, the intertooth activity would be classified as an SMC by definition. It is therefore evident that SMCs and sawtooth events can be viewed as related phenomena. We suggest that the the level of external driving and/or the level of external IMF/SW fluctuations may determine whether an SMC or a sawtooth event develops.

[90] On the question of tooth triggering, we found that some of the teeth were clearly correlated with fluctuations in either the IMF or SW (or both), while for other teeth there was no obvious correlation (see Table 2). Conversely, we observed numerous fluctuations in the IMF and/or SW at times between the tooth onsets. Although *Lyons et al.* [2005] and *Lee et al.* [2005] have proposed that potential triggers can become nullified under certain conditions (e.g., a northward turning combined with a pressure reduction produces no trigger), it is not clear that all of the intertooth fluctuations can be categorized as null events. For example, there are multiple pressure pulses associated with the 0413 UT event (which do not appear to be null events), but there is only a single major tooth-like response (with some smaller dispersionless fluctuations superimposed). In addition, the 2302:25 UT (10 August) event only appears to be associated with positive deflection in B_Y at ACE which would not normally be considered a trigger, but a tooth develops nevertheless. It is also interesting to note that one of the strongest examples of a null event in the *Lyons et al.* [2005] study occurred just prior to 1000 UT on 11 August. They identified this as a null event because Geotail apparently showed a large northward turning combined with a strong reduction in the solar wind pressure. Thus they claim that a tooth was averted by this null effect. However, it is important to note that in their study *Lyons et al.* [2005] appear to have used GSM coordinates for the ACE data and GSE coordinates for the Geotail data. It appears that the coincident large increase in B_Y at this time results in a B_Z increase in GSE coordinates but not in GSM coordinates. This can be seen by comparing our Figure 24 (all in GSM) with Figure 5 presented by *Lyons et al.* [2005]. Since, in GSM coordinates, the IMF variations for this event would not be considered a typical trigger it is questionable whether the pressure reduction provided a nullifying effect.

[91] Given that there are considerably more variations in the SW/IMF than there are teeth, it appears that once a tooth is initiated, the magnetosphere becomes unresponsive (in a major way) to these fluctuations for a typical 2–4 hour intertooth period. This is consistent with the idea that the teeth represent a nonlinear substorm-like reconfiguration of the magnetosphere and strongly argues against the hypothesis that the teeth are produced as a “directly driven” response to solar wind pressure variations as suggested by *Lee et al.* [2004]. Instead, we suggest that any spectrum of solar wind disturbances (that are sufficiently closely spaced in time) will lead to the observed periodicity because the internal stability threshold for substorm triggering is only breached during the late growth phase of each substorm.

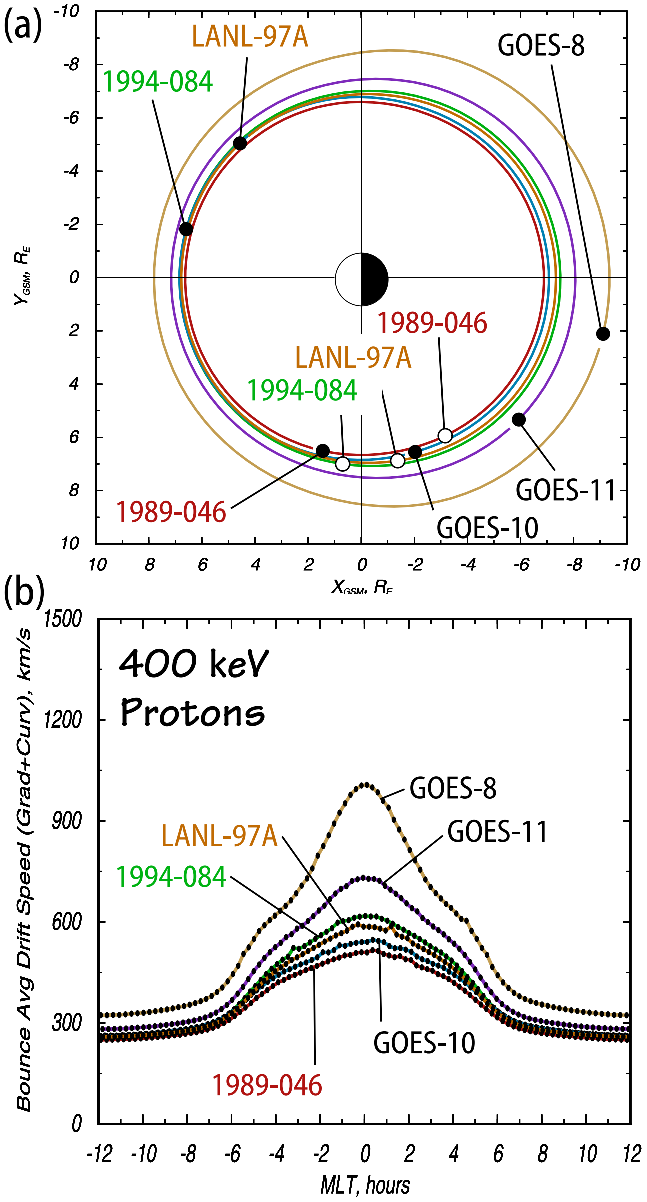

Figure 28. Drift shells for 45° particles for the geosynchronous spacecraft at 0413 UT on 11 August 2000. The T89 $K_p = 5$ model was used. The black circles represent the projection (along field lines) of the spacecraft location to the minimum B surface of each drift shell. The white circles represent the location of the injection boundary derived from the observed drift of 400 keV protons.

This hypothesis is much more consistent with the recent studies of *Huang et al.* [2004b, 2005] and *Henderson et al.* [2006], and we agree with many of the objections raised by *Huang et al.* [2005] regarding the *Lee et al.* [2004] study.

[92] Finally, to illustrate that it is not unreasonable to attribute the observed delay times to substorm injections, we show the (T89 $K_p = 5$ model) drift shells for particles with 45° pitch angles that each of the geosynchronous spacecraft were on at 0413 UT in Figure 28a. Figure 28b shows the corresponding bounce-averaged gradient and curvature drift speed for 400 keV protons (45° pitch angle) in each of these shells. The black circles in Figure 28a are the spacecraft locations projected along field lines to the minimum B surface of each drift shell. On the basis of an onset time of 0413:28 UT and the observed arrival times in the P5 channel at 1989-046, 1994-084, and LANL-97A, the western edge of the injection region within each shell is inferred to be at the location of the white circles. Note that the drift shells are not the same for each spacecraft and that the drift speed can be much greater on the nightside than on the dayside. From this crude calculation, we can see that the injection region appears to follow a classic spiral-like geometry in the dusk to midnight sector.

[93] However, we note that there is considerable uncertainty in these results for at least four reasons. (1) Although the flux increases appear to occur very abruptly in Figures 1 and 4, it is actually quite difficult to measure the true arrival times to subminute accuracy due to the presence of numerous small-scale fluctuations. (2) The SOPA data is spin averaged (i.e., it includes many pitch angles) and we have only computed drift shells for particles with 45° pitch angles. (3) Although the T89 model is more realistic than a dipole, the real field is certainly quite different during sawtooth events, and it is time varying. (4) The injection region itself may be dynamic (e.g., it may propagate inward and/or expand in azimuth). In order to robustly determine the injection regions associated with sawtooth events, these issues need to be properly addressed.

[94] On the basis of the observations presented here and elsewhere [e.g., *Reeves et al.*, 2003; *Huang et al.*, 2003a; *Henderson*, 2004; *Henderson et al.*, 2006; *Huang*, 2005; *Kitamura et al.*, 2005], we conclude that the majority of the individual teeth comprising sawtooth events are in fact substorms. In addition, we found that some apparent tooth-like flux increases (particularly in energetic protons) can be produced by solar wind shocks and can result in a magnetospheric response that is quite different from that of a substorm. Since there are typically more potential IMF/SW triggers available during sawtooth events, we propose that the periodicity results because the magnetosphere only becomes susceptible to (external or internal) triggering once it is driven beyond some stability threshold (or enters a "metastable" configuration). A simple analog of this scenario is shown in Figure 29 in terms of a stochastic potential well. During SMCs, we hypothesize that substorms are averted because the magnetosphere is able to process the energy input in a quasi-continuous manner without

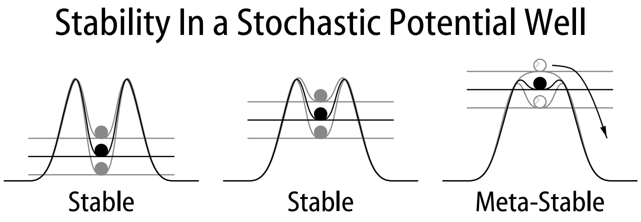

Figure 29. Schematic representation of stability in a stochastic potential well. The configuration remains stable to stochastic fluctuations of a given amplitude provided the well is deep enough. Sawtooth events may evolve toward the metastable configuration over a 2–4 hour period and become susceptible to external or internal triggering.

approaching a configuration of marginal stability. In addition, lower levels of external fluctuations (i.e., potential triggers) may contribute to SMC-like behavior.

[95] Note that it is highly likely that not all teeth, even ones associated with clear dispersed injection signatures, are in fact substorms. Other processes, like poleward boundary intensifications combined with equatorward ejection of auroral forms (east-west inclined arcs and streamers) also appear to be able to produce sawtooth-like particle injections. Investigation of this type of disturbance will be deferred to a future study.

[96] **Acknowledgments.** This research was supported at Los Alamos National Laboratory by NSF GEM grant ATM-0202303. The Sym-H, AU, AL, and much of the 1-min resolution ground magnetometer data were provided by the World Data Center for Geomagnetism at Kyoto University. The Polar magnetic field data were obtained via the UCLA online data server, and we thank C. Russell for making this data available there. The PCN index was obtained from the World Data Center for Geomagnetism, Copenhagen. The high-resolution 1 s 210 MM magnetometer data were kindly provided by K. Shiokawa from the Solar-Terrestrial Environment Laboratory, Nagoya University. The authors also wish to thank the SAMNET team for magnetometer data. SAMNET is a PPARC National Facility operated by Lancaster University. The 5 s resolution Canadian CARISMA magnetometer data were obtained from the Space Science Data Portal, and we thank the principal investigator, Ian Mann, for making it available. The ACE, Geotail, and Wind IMF and SW data were obtained from the NASA CDAWeb.

[97] Arthur Richmond thanks Chao-Song Huang and Dae-Young Lee for their assistance in evaluating this paper.

References

Akasofu, S. I. (1964), The development of the auroral substorm, *Planet. Space Sci.*, *12*, 273–282.

Akasofu, S. I. (1977), *Physics of Magnetospheric Substorms*, Springer, New York.

Akasofu, S. I., J. Kisabeth, G. J. Romick, H. W. Kroehl, and B. H. Ahn (1980), Day-to-day and average magnetic variations along the IMS Alaska Meridian chain of observatories and modeling of a 3-dimensional current system, *J. Geophys. Res.*, *85*, 2065–2078.

Allen, J. H., and H. W. Kroehl (1975), Spatial and temporal distributions of magnetic effects of auroral electrojets as derived from AE indices, *J. Geophys. Res.*, *80*, 3667–3677.

Baker, D. N., et al. (1993), CDAW 9 analysis of magnetospheric events on May 3, 1986: Event C, *J. Geophys. Res.*, *98*, 3815–3834.

Belian, R. D., T. E. Cayton, and G. D. Reeves (1995), Quasi-periodic, substorm associated, global flux variations observed at geosynchronous orbit, in *Space Plasmas: Coupling Between Small and Medium Scale Processes*, *Geophys. Monogr. Ser.*, vol. 86, edited by M. Ashour-Abdalla, T. Chang, and P. Dusenbery, p. 143, AGU, Washington, D. C.

Clauer, C. R., X. Cai, D. Welling, A. DeJong, and M. G. Henderson (2006), Characterizing the 18 April 2002 storm-time sawtooth events using ground magnetic data, *J. Geophys. Res.*, *111*, A04590, doi:10.1029/2005JA011099.

Gjerloev, J. W., R. A. Hoffman, M. M. Friel, L. A. Frank, and J. B. Sigwarth (2004), Substorm behavior of the auroral electrojet indices, *Ann. Geophys.*, *22*(6), 2135–2149.

Henderson, M. G. (2004), The May 2–3 1986 CDAW–9C interval: A sawtooth event, *Geophys. Res. Lett.*, *31*(1), L11804, doi:10.1029/2004GL019941.

Henderson, M. G., L. Kepko, H. E. Spence, M. Connors, J. B. Sigwarth, L. A. Frank, H. J. Singer, and K. Yumoto (2002), The evolution of north-south aligned auroral forms into auroral torch structures: The generation of omega bands and ps6 pulsations via flow bursts, in *Proceedings of the Sixth International Conference on Substorms*, edited by R. M. Winglee, p. 169, Univ. of Wash., Seattle.

Henderson, M. G., G. D. Reeves, R. Skoug, M. F. Thomsen, M. H. Denton, S. B. Mende, T. J. Immel, P. C. Brandt, and H. J. Singer (2006), Magnetospheric and auroral activity during the April 18, 2002 sawtooth event, *J. Geophys. Res.*, *111*, A01S90, doi:10.1029/2005JA011111.

Hess, W. N. (1968), *The Radiation Belts and Magnetosphere*, 34 pp., Blaisdell, Waltham, Mass.

Huang, C. S. (2002), Evidence of periodic (2–3 hour) near-tail magnetic reconnection and plasmoid formation: Geotail observations, *Geophys. Res. Lett.*, *29*(24), 2189, doi:10.1029/2002GL016162.

Huang, C. S. (2005), Variations of polar cap index in response to solar wind changes and magnetospheric substorms, *J. Geophys. Res.*, *110*, A01203, doi:10.1029/2004JA010616.

Huang, C. S., J. C. Foster, G. D. Reeves, G. Le, H. U. Frey, C. J. Pollock, and J. M. Jahn (2003a), Periodic magnetospheric substorms: Multiple space-based and ground-based instrumental observations, *J. Geophys. Res.*, *108*(A11), 1411, doi:10.1029/2003JA009992.

Huang, C. S., G. D. Reeves, J. E. Borovsky, R. M. Skoug, Z. Y. Pu, and G. Le (2003b), Periodic magnetospheric substorms and their relationship with solar wind variations, *J. Geophys. Res.*, *108*(A6), 1255, doi:10.1029/2002JA009704.

Huang, C. S., J. C. Foster, G. D. Reeves, J. L. Chau, K. Yamoto, and K. Kitamura (2004a), Variations of low-latitude geomagnetic fields and Dst index caused by magnetospheric substorms, *J. Geophys. Res.*, *109*, A05219, doi:10.1029/2003JA010334.

Huang, C. S., G. Le, and G. D. Reeves (2004b), Periodic magnetospheric substorms during fluctuating interplanetary magnetic field Bz, *Geophys. Res. Lett.*, *31*, L14801, doi:10.1029/2004GL020180.

Huang, C. S., G. D. Reeves, G. Le, and K. Yumoto (2005), Are sawtooth oscillations of energetic plasma particle fluxes caused by periodic substorms or driven by solar wind pressure enhancements?, *J. Geophys. Res.*, *110*, A07207, doi:10.1029/2005JA011018.

Immel, T. J., J. D. Craven, and A. C. Nicholas (2000), An empirical model of the OI FUV dayglow from DE-1 images, *J. Astron. Sol. Terr. Phys.*, *62*, 47–64.

Kamide, Y. (1988), *Electrodynamic Processes in the Earth's Ionosphere and Magnetosphere*, Kyoto Sangyo Univ., Kyoto, Japan.

Kan, J. R., and L. C. Lee (1979), Energy coupling function and solar wind-magnetosphere dynamo., *Geophys. Res. Lett.*, *6*, 577–580.

Kitamura, K., H. Kawano, S. Ohtani, A. Yoshikawa, and K. Yumoto (2005), Local time distribution of low and middle latitude ground magnetic disturbances at sawtooth injections of 18–19 April 2002, *J. Geophys. Res.*, *110*, A07208, doi:10.1029/2004JA010734.

Lee, D., and L. R. Lyons (2003), Sawtooth oscillations directly driven by solar wind dynamic pressure enhancements, *Eos. Trans. AGU*, *84*(46), Fall Meet. Suppl., Abstract SM32B-1149.

Lee, D., and L. R. Lyons (2004), Geosynchronous magnetic field response to solar wind dynamic pressure pulse, *J. Geophys. Res.*, *109*, A04201, doi:10.1029/2003JA010076.

Lee, D., L. R. Lyons, and K. Yumoto (2004), Sawtooth oscillations directly driven by solar wind dynamic pressure enhancements, *J. Geophys. Res.*, *109*, A04202, doi:10.1029/2003JA010246.

Lee, D., L. R. Lyons, and G. D. Reeves (2005), Comparison of geosynchronous energetic particle flux responses to solar wind dynamic pressure enhancements and substorms, *J. Geophys. Res.*, *110*, A09213, doi:10.1029/2005JA011091.

Liou, K., J. F. Carbary, P. T. Newell, C. I. Meng, and O. Rasmussen (2003), Correlation of auroral power with the polar cap index, *J. Geophys. Res.*, *108*(A3), 1108, doi:10.1029/2002JA009556.

Lui, A. T. Y., T. Hori, S. Ohtani, Y. Zhang, X. Y. Zhou, M. G. Henderson, T. Mukai, H. Hayakawa, and S. B. Mende (2004), Magnetotail behavior during storm time "sawtooth events", *J. Geophys. Res.*, *109*, A10215, doi:10.1029/2004JA010543.

Lyons, L. R., D. Y. Lee, C. P. Wang, and S. B. Mende (2005), Global auroral responses to abrupt solar wind changes: Dynamic pressure, substorm, and null events, *J. Geophys. Res.*, *110*, A08208, doi:10.1029/2005JA011089.

Mauk, B. H., and C. I. Meng (1983), Dynamical injections as the source of near geostationary quiet time particle spatial boundaries, *J. Geophys. Res.*, *88*, 10,011–10,024.

Minenko, L. V., P. A. Sedykh, and V. M. Mishin (2000a), The chain of recurrent substorms on May 3, 1986, and magnetotail length fluctuations, in *Proceedings of the Fifth International Conference on Substorms*, edited by A. Wilson, pp. 59–62, ESA Publ. Div., Noordwijk, Netherlands.

Minenko, L. V., P. A. Sedykh, and V. M. Mishin (2000b), Timing of a chain of substorms on May 3, 1986, in *Proceedings of the Fifth International Conference on Substorms*, edited by A. Wilson, pp. 527–530, ESA Publ. Div., Noordwijk, Netherlands.

Murphree, J. S., R. D. Elphinstone, M. G. Henderson, L. L. Cogger, and D. J. Hearn (1993), Interpretation of optical substorm onset observations, *J. Astron. Terr. Phys.*, *55*(8), 1159–1170.

Olson, J. V., and G. Rostoker (1977), Latitude variation of the spectral components of auroral zone Pi2, *Planet. Space Sci.*, *25*(7), 663–671.

Opgenoorth, H. J., M. A. L. Persson, T. I. Pulkkinen, and R. J. Pellinen (1994), Recovery phase of magnetospheric substorms and its association with morning-sector aurora, *J. Geophys. Res.*, *99*, 4115–4129.

Pulkkinen, T. I., et al. (1991), Modeling the growth-phase of a substorm using the Tsyganenko model and multi-spacecraft observations—CDAW-9, *Geophys. Res. Lett.*, *18*, 1963–1966.

Reeves, G. D., et al. (2003), Image, Polar, and geosynchronous observations of substorm and ring current ion injection, in *Disturbances in Geospace: The Storm-Substorm Relationship*, *Geophys. Monogr. Ser.*, vol. 142, edited by A. S. Sharma, Y. Kamide, and G. S. Lakhina, pp. 91–101, AGU, Washington, D. C.

Rostoker, G. (1966), Midlatitude transition bays and their relation to spatial movement of overhead current systems, *J. Geophy. Res.*, *71*, 79–95.

Thomsen, M. F., E. Noveroske, J. E. Borovsky, and D. J. McComas (1999), Calculation of moments from measurements by the Los Alamos magnetospheric plasma analyzer, *Tech. Rep. LA–13566–MS*, Los Alamos Natl. Lab., Los Alamos, N. M.

Troshichev, O. A., and R. Y. Lukianova (2002), Relation of PC index to the solar wind parameters and substorm activity in time of magnetic storms, *J. Atmos. Sol. Terr. Phys.*, *64*, 585–591.

Troshichev, O. A., N. P. Dmitrieva, and B. M. Kuznetsov (1979), Polar cap magnetic activity as a signature of substorm development, *Planet. Space Sci.*, *27*(3), 217–221.

Troshichev, O. A., V. G. Andrezen, S. Vennerstrom, and E. Friischristensen (1988), Magnetic activity in the polar cap—A new index., *Planet. Space Sci.*, *36*(11), 1095–1102.

Troshichev, O. A., R. Y. Lukianova, V. O. Papitashvili, F. J. Rich, and O. Rasmussen (2000), Polar cap index (PC) as a proxy for ionospheric electric field in the near-pole region, *Geophys. Res. Lett.*, *27*, 3809–3812.

Weimer, D. R., D. M. Ober, N. C. Maynard, W. J. Burke, M. R. Collier, D. J. McComas, N. F. Ness, and C. W. Smith (2002), Variable time delays in the propagation of the interplanetary magnetic field, *J. Geophys. Res.*, *107*(A8), 1210, doi:10.1029/2001JA009102.

M. H. Denton, Solar-Terrestrial Physics Group, School of Physics and Astronomy, University of Southampton, Highfield, Southampton SO17 1BJ, UK.

E. Donovan, Department of Physics and Astronomy, University of Calgary, Calgary, AB, Canada T2N 1N4.

L. A. Frank, Department of Physics and Astronomy, 212 Van Allen Hall, University of Iowa, Iowa City, IA 52242-1479, USA.

M. G. Henderson, G. D. Reeves, R. Skoug, and M. F. Thomsen, Los Alamos National Laboratory, MS D-466, Los Alamos, NM 87545, USA. (mghenderson@lanl.gov)

T. J. Immel and S. B. Mende, Space Sciences Laboratory, University of California, Berkeley, 7 Gauss Way, Berkeley, CA 94720, USA.

R. L. McPherron, Department of Earth and Space Sciences, University of California, Los Angeles, 595 Charles Young Drive East, Box 951567, Los Angeles, CA 90095, USA.

J. B. Sigwarth, NASA Goddard Space Flight Center, Code 696, Building 21, Room 232, Greenbelt, MD 20771, USA.

H. J. Singer, Space Environment Center, NOAA, 325 Broadway, Boulder, CO 80305, USA.